Numerical Simulations of the 29 June 2000 STEPS Supercell: Microphysics, Electrification, and Lightning

Kristin M. Kuhlman
School of Meteorology, University of Oklahoma, Norman, OK U.S.A.

Conrad L. Ziegler
National Severe Storms Laboratory, Norman, OK U.S.A.

Edward R. Mansell
Cooperative Institute for Mesoscale Meteorological Studies (CIMMS)
University of Oklahoma, Norman, OK U.S.A.

Donald R. MacGorman
National Severe Storms Laboratory, Norman, OK U.S.A

Jerry M. Straka
School of Meteorology, University of Oklahoma, Norman, OK U.S.A.

to be Submitted to Monthly Weather Review
May 11, 2005

Abstract

A three-dimensional dynamic cloud model incorporating airflow dynamics, microphysics, and thunderstorm electrification mechanisms was used to simulate the first three hours of the 29 June 2000 supercell from the Severe Thunderstorm Electrification and Precipitation Study (STEPS). The 29 June storm contained high flash rates and produced predominately positive cloud-to-ground lightning, large hail, and an F1 tornado. Four different simulations of the storm were made, each one containing a different noninductive (NI) charging parameterization. The charge structure and thus lightning polarity of the simulated storm was sensitive to the treatment of cloud water dependence in the different NI charging schemes. The results from the simulations are compared with observations from STEPS, including balloon-borne electric field meter soundings and flash locations from the Lightning Mapping Array. The observed "inverted" tripolar charge structure, which features a main positive charge region with lower and upper negative charge regions, was well approximated by the model. The polarity of the ground flashes was opposite that of the lowest charge region of the inverted tripole in both the observed storm and the simulations. The convective intensity of the storm was indicated by the total flash rate in both the observations and simulations. Rather high correlations existed between the detrended time series for graupel volume and total flash rate. Updraft volume and updraft mass flux also were well correlated with total flash rate, though there was little correlation between total flash rate and maximum updraft speed. Based on these correlations, it is likely that the best electrical representation of a storm that is reliable for storm intensity is the total flash rate.

1. Introduction

Supercell thunderstorms have been the focus of extensive research due to their complexity and their propensity for producing severe weather. A recent field project, the Severe Thunderstorm Electrification and Precipitation Study (STEPS), took place during 2000 to study severe storms in the High Plains of the United States. One of the main goals of the project was to achieve a better understanding of the interactions among storm kinematics, microphysics, and electrification (NCAR/MMM, 2000). Numerous storms–including supercells, short-lived multicell storms, and large mesoscale convective complexes–were observed and documented during STEPS.

An in-depth study of storm processes proceeds from a combination of observations and numerical simulations. STEPS provided a comprehensive observational dataset for detailed comparison with numerical simulations of storm evolution. This study focuses on numerical simulations of the 29 June STEPS supercell that produced an F1 tornado and predominately positive ground flashes. The objective is to evaluate the simulated charge structure, lightning flash rate, and polarity in the context of the observed storm and to determine the sensitivity of the modeled storm to electrification parameterizations. The origins of positive cloud-to-ground (CG) flashes and the relationships between the modeled total flash rate and storm characteristics are of particular interest.

a. Previous electrification studies

Early measurements of the surface electric field revealed evidence of a dipolar charge structure within thunderstorms (Fig. 1a). As observing technology improved, investigations increasingly emphasized in-situ measurements at altitude in thunderstorms, revealing a tripolar charge structure–a dipole with a lower positive charge region (Fig. 1b). In more recent investigations, a screening layer was added to the overall dipolar or tripolar charge distribution.

Several studies have suggested that dipole or tripole models are not sufficient to describe how charge is distributed in all thunderstorms. Rust and Marshall (1996) argued that the current tripole models are too simplistic to apply to all mature thunderstorms and mesoscale convective systems. A more complex charge structure consisting of four main charge regions near the updraft and six charge regions outside the updraft in the convective precipitation region was suggested by Stolzenburg et al. (1998). Other researchers have argued that the tripole is adequate to describe the

basic thunderstorm charge structure and believe that abandonment of the tripole model would be "ill-advised" (Williams 2001).

The concept of an inverted (or reversed polarity) dipole (Fig. 1c) was discussed by Seimon (1993) for the Plainfield, Illinois supercell that displayed an anomalously high number of positive ground flashes. The existence of an inverted tripole (Fig. 1d) was first introduced by Marshall et al. (1995a) based on electric field soundings in a strong storm near Dalhart, Texas. It was suggested that positive CG flashes in the Dalhart storm immediately following the sounding may have been initiated due to the inverted charge structure of the storm.

The first documentation of severe storms that commonly produce positive CG flashes was provided by Rust et al. (1981). They found that positive CG flashes originated from both the anvil and mesocyclone areas, and concluded that positive CG flashes may indicate storm severity. Williams (2001) discussed several hypotheses regarding the orgins of charge in positive ground flashes, including tilting of the charge layers due to wind shear, precipitation unshielding (i.e., fallout of a lower-level negative charge region revealing the upper positive charge), and convective feedback based on Vonnegut (1963).

Several studies have examined correlations between positive ground flashes and severe weather. Seimon (1993) noted positive ground flashes preceeding an F5 tornado, while MacGorman and Burgess (1994) showed that damaging tornadoes occurred after peaks in positive CG flashes. However, positive ground flashes may prove ineffective as a severe weather indicator unless correlations can be shown to be reliable (Branick and Doswell 1992; Perez et al. 1997). Further study is needed to identify the source of positive ground flashes and their relation to the charge structure and severity of the parent storm.

Laboratory experiments have attempted to reproduce the process of charge transfer in storms. The laboratory studies have shown that temperature, liquid water content, the sizes of the particles, and the riming rate all exert important influences on charging. Reynolds et al. (1957) and Takahashi (1978) were among the first to examine the charge separated per rebounding collision of graupel and ice to determine how hydrometeors obtained charge in the mixed-phased region commonly present in storms. Jayaratne et al. (1983) and Keith and Saunders (1990) also investigated charge separation, including dependency on crystal size, impact velocity, and contaminants in water particles. A broad agreement is noticed between the laboratory results, with differences

depending on the laboratory apparatus used (Jayaratne 1993; Pereyra et al. 2000), the growth mode of the ice crystals, and the liquid water content (MacGorman and Rust 1998, pp. 67-69).

Several studies have used numerical cloud models to further test the implications of laboratory measurements for storm electrification. Takahashi (1983, 1984) parameterized his laboratory noninductive charging data in a two-dimensional, time dependent axisymmetric model study of small thunderstorms. Mitzeva and Saunders (1990) added a parameterization of the laboratory results of Jayaratne et al. (1983) and Keith and Saunders (1990) to a one-dimensional model to examine the evolution of charging rates in three different simulations. Ziegler et al. (1986) used a one-dimensional kinematic model with an electrification mechanism suggested by Gardiner et al. (1985). Ziegler et al. (1991) expanded their kinematic model to three-dimensions with time dependence and included a screening layer parameterization. The three-dimensional kinematic model was later applied by Ziegler and MacGorman (1994) to study a supercell storm. Mansell (2000) and Mansell et al. (2002) developed a lightning parameterization using a stochastic dielectric breakdown model that simulates the stepwise progression of individual flashes and reduces the electric field by realistically redistributing charge from the flash channel into the model domain. Mansell et al. (2005) examined the sensitivity of charge structure and lightning to a range of NI charging parameterizations in a three-dimensional multicell storm simulation.

Correlations of flash rate with various microphysical parameters have been the focus of many studies as flash rate is often considered an indication of storm severity. One of the most obvious and perhaps important parameters controlling flash rate is the storm size (Williams 2001). Large storms tend to have a higher sustained flash rate due to a stronger updraft (MacGorman et al. 1989), though there are documented cases of smaller storms with strong updrafts having relatively high flash rates. High reflectivity (Lhermitte and Krehbiel 1979), graupel volume (Carey and Rutledge 1996) and production of large hail (Carey and Rutledge 1998) have also been related to flash rate.

b. Goals of this research

This study examines the consequences of different charge separation mechanisms on simulated electrification and compares the simulated charge structures to the observed charge structure of the well-documented 29 June 2000 STEPS storm. An analogous study has been performed using a two-dimensional model of the 19 July 1981 Cooperative Convective Precipitation Experiment

(CCOPE) storm (Helsdon et al. 2001), in which three different noninductive charging schemes were examined. Results from the Helsdon et al. (2001) study suggested the laboratory results from Takahashi might be the best representation of NI charging. Mansell et al. (2005) and Mansell et al. (2002) tested different numerical parameterizations of noninductive and inductive charging in a small multicellular storm. The present study will determine which charging scheme(s) provide similar results for the observed morphology of the 29 June 2000 storm.

There has been considerable discussion about cloud-to-ground flashes and their relationship to the charge distribution and severity of storms. The present study examines multiple positive CG flashes that occur at various times during both the simulations and the observed storm and relates these positive CG flashes to the evolving kinematic, microphysical and electrical structure of the storm.

Another point of interest is the relationships between the flash rate and the storm characteristics in the simulations. Several investigators have found relationships in observed storms between reflectivity or updraft strength and total flash rate (MacGorman et al, 1989). Baker et al. (1995) and Solomon and Baker (1998) examined the total flash rate in conjunction with updraft speed, reflectivity, precipitation rate, ice concentration, and cloud radius in a one-dimensional model. The present study employs a three-dimensional model to further examine the relationships between flash rate and other storm properties such as updraft speed and mass flux, precipitation rate, graupel volume, and rain mass.

2. Model Description

a. Dynamics and microphysics

The dynamic cloud model is described in detail by Straka (1989) and Carpenter et al. (1998). The model is three dimensional, non-hydrostatic and fully compressible, and is based on the set of equations from Klemp and Wilhelmson (1978). The model includes prognostic equations for velocity components (momentum), perturbation pressure, potential temperature, turbulent kinetic energy, water vapor and hydrometeor mixing ratios, rime history, and charge variables.

The model employs a microphysics package that includes two liquid hydrometeor categories and ten ice categories distinguished by particle density, habit, and size (Straka and Mansell 2005).

Fractions of mass may move from one category to another depending on droplet collection, riming rate, and melting. Source and sink terms for form and phase changes are included in the microphysics scheme for condensation and evaporation, deposition and sublimation, freezing and melting, aggregation and nucleation, and riming of ice particles, graupel and hail.

b. Charging and electrification

The model includes a choice of parameterizatons for hydrometeor charging (Mansell et al. 2005). This study uses both inductive and noninductive charging for electrification. The results of laboratory and modeling studies strongly suggest that noninductive charging plays the primary role in producing electrification rates and magnitudes close to those of observed storms (MacGorman and Rust 1998). However, it is believed that inductive charging could also play a role (Brooks and Saunders 1994). Inductive charging occurs in the presence of an electric field when a rebounding collision occurs between two polarized particles. In the model, inductive charging is only included during graupel-droplet collisions when graupel are in dry growth mode. Noninductive charging (i.e., independent of the electric field) occurs with rebounding collisions between riming graupel and ice particles in the presence of cloud droplets. The macroscopic spatial separation of opposite charges on cloud and precipitation particles from the combined effect of their differential fall speeds and wind shear subsequently generate fields strong enough to produce lightning.

Inductive charging in the model is calculated based on a formula from Ziegler et al. (1991). This equation is expressed by Mansell et al. (2005) in terms of characteristic diameter D_g and mass weighted mean fallspeed $\bar{V}_g$ of graupel as:

$$\begin{aligned} \frac{\partial \varrho_g}{\partial t} &= (\pi^3/8)\left(\frac{6.0\bar{V}_g}{\Gamma(4.5)}\right) E_{gc} E_r n_{t,c} n_{0g} D_c^2 \times \\ &\quad \left[\pi\Gamma(3.5)\epsilon\langle\cos\theta\rangle E_z \mathcal{D}_{n,g}^2 - \Gamma(1.5)\varrho_g/(3n_{t,g})\right]. \end{aligned} \tag{1}$$

In eq. 1, E_{gc} and E_r are the collection and rebound efficiencies, $n_{t,c}$ and $n_{t,g}$ are the total cloud water and graupel number densities, $n_{0,g}$ is the number concentration intercept for graupel, D_c is the cloud droplet diameter, $\langle\cos\theta\rangle$ is the average cosine of the angle of the rebounding collision, E_z is the vertical component of the electric field, ϱ_g is the charge on graupel, and ϵ is the permittivity of air. The inductive charging used in the simulations approaches values described as "strong" by

Mansell et al. (2005), with $E_r = 0.01$ and $\langle \cos\theta \rangle = 0.45$.

Noninductive charging involving riming graupel and ice crystals has been the focus of several laboratory experiments. The charge gained by the graupel is dependent on the ambient temperature and the liquid water content as well as the size and growth state of the hydrometeors. Several studies have focused on a reversal temperature for the transition of sign of the charge gained by the graupel. Most investigators agree that the reversal temperature is dependent on the liquid water content or riming rate, though differences arise in determining the conditions for charging sign reversal. The general formula for noninductive charge separation between colliding particles x and y is:

$$\frac{\partial \varrho_{xy}}{\partial t} = \int_0^\infty \int_0^\infty \frac{\pi}{4} \delta q'_{xy} (1 - E_{xy}) |V_y - V_x| \times (D_x + D_y)^2 n_x(D_x) n_y(D_y) dD_x dD_y, \qquad (2)$$

where D_x and D_y are the diameters of the colliding particles, E is the collection efficiency, $|V_y - V_x|$ is the relative fall speed, n is the number concentration, and $\delta q'_{xy}$ is the charge separated per collision. A representative weighted average separated charge per collision, δq_{xy}, replaces $\delta q'_{xy}$. Thus, eq. 2 is simplified by permitting δq_{xy} to be moved outside the integral (Mansell et al. 2005). The magnitude of δq_{xy} is limited to a maximum of 50 fC for graupel-snow collisions and 20 fC for graupel-cloud ice collisions to prevent unrealistic charging and lightning rates. For this study, the model includes four different parameterizations of the noninductive charging process as each varies in determining the sign and level of charging.

1). NONINDUCTIVE CHARGING PARAMETERIZATIONS

The noninductive charging rate in the Saunders and Peck (1998) scheme (SP98) is based on a critical rime accretion rate (RAR) from their measurements. The temperature-dependent critical RAR value (RAR_{crit}) defines positive and negative charging regions (Fig. 2a). The sign of the charge transferred to the graupel during a rebounding collision in the SP98 scheme is strongly influenced by the amount of water accreted on the graupel (i.e. the rimer). The Riming Rate (RR) scheme, as described in Mansell et al. (2005), is developed in a similar fashion to that of SP98. It is also based on a critical rime accretion rate, but with a slightly different temperature and liquid water dependence (Fig. 2b).

The Takahashi (TAKA) charging scheme is based on the laboratory work of Takahashi (1978). The polarity of charge gained by graupel is determined by the cloud water content and temperature (Fig. 2c). For the model parameterization, the results are taken from a lookup table developed by Wojcik (1994), with additions from Takahashi (1984) for variation in the charge separation per collision which is dependent on impact velocity and crystal size. The charge separated per collision at temperatures between 0° C and -30° C and liquid water content from 0.01 to $30\,\mathrm{g\,m^{-3}}$ are included in the table. At temperatures below -30° C the charge separated per collision is the value at -30° C.

The final noninductive parameterization used is the Gardiner/Ziegler (GZ) scheme. This scheme is based on the laboratory results of Jayaratne et al. (1983), as adapted from Gardiner et al. (1985) by Ziegler et al. (1986, 1991). The dependence on liquid water content is given by an adjustable reversal temperature, T_r, and the cloud water mixing ratio. At temperatures below T_r, graupel (ice) charges negatively (positively) and at higher temperatures the sign of charging is reversed. In the present study, the reversal temperature is set to -15°C (Fig. 2d).

2). CHARGE CONSERVATION, ADVECTION, AND IONS

A charge density is connected with every hydrometeor type. As mass shifts between categories in the microphysics, the charge also is transferred from one category to another (e.g. mass from ice to rain). Although charge is conserved in the model domain, charge is not absolutely conserved due to charge movement from ion currents entering or exiting the domain, advection through a lateral boundary, or by cloud-to-ground lightning. The charge continuity equation from Mansell et al. (2005) resembles a typical conservation equation with treatment of advection, diffusion, and falling particle motion. The model neglects the accelerations of charged particles in an electric field. The electric field is determined as the negative gradient of the potential: $\mathbf{E} = -\nabla\phi$.

Explicit treatment of ions has recently been added to the OU-NSSL model by Mansell et al. (2005). Conservation equations are defined for both positive and negative ion concentrations. The equations take into account advection and mixing, drift motion (ion motion induced by the electric field), cosmic ray generation, ion recombination, ion attachment to hydrometeors, corona discharge from the surface, and release of ions from evaporating hydrometeors. Mansell et al. (2005) use a fair weather state from Gish (1944) as expressed by Helsdon and Farley (1987).

3). LIGHTNING PARAMETERIZATION

Lightning flashes are parameterized by a stochastic dielectric breakdown model (Mansell et al. 2002). The lightning develops bidirectionally across a uniform grid with each step chosen randomly from among the surrounding points at which the electric field meets or exceeds a threshold value for propagation. After each step, the electric field is calculated to determine the contribution by the lightning channel. The resulting flash has a branched or fractal-like leader structure in three dimensions.

Flash initiation occurs if the electric field exceeds the macroscopic "break-even" electric field threshold $E_{\rm be}$ (Marshall et al. 1995a). A particular initiation point is chosen randomly from all the points that exceed $0.9E_{\rm be}$ and each channel maintains an overall charge neutrality as long as neither end goes to ground. Positive leaders carry positive charge and travel preferentially through negative charge regions, while negative leaders carry negative charge and tend to travel through regions of net positive charge (Mansell et al. 2002). Therefore, the simulated flashes tend to reflect the simulated charge structure.

3. Observed and simulated 29 June storm evolution

a. The 29 June 2000 supercell storm

The 29 June 2000 supercell storm formed just ahead of a dryline with an approaching mesoscale cold front to the north (Fig. 3a). The storm's first radar echo appeared around 2130 UTC (all times are Universal Time) near the borders of Colorado, Nebraska and Kansas (Fig. 3b). The storm lasted approximately four hours, moving southeastward through northwest Kansas (Fig. 3b) before being overtaken by part of a mesoscale convective system (MCS) in central Kansas later that evening. During the first three hours, the storm produced large hail, an F1 tornado, and a profuse amount of lightning. As the storm moved through the STEPS domain, it was observed by a network of Doppler radars, a T-28 armored research airplane, balloon soundings of the electric field, and the Lightning Mapping Array (LMA). The LMA is a GPS-based system that locates sources of VHF radiation from lightning discharges in three spatial dimensions and time (Rison et al. 1999; Krehbiel et al. 2000). The balloon borne electric field meter (EFM) measures the vector electric field, **E** (as described by Winn et al. 1978; Marshall et al. 1995b; Coleman et al. 2003).

Atmospheric conditions in the storm environment supported supercell storm development (Johns and Doswell 1992; Weisman and Klemp 1982). Environmental winds near the storm were from the south and veered to the west with height as shown in the 2022 NCAR GLASS sounding from Goodland, KS (Fig. 4). The sounding was released 40 miles to the southeast of the storm initiation, and one hour before it was first detected by radar. Although the environment was unstable as depicted by the 1319 J kg^{-1} of convective available potential energy (CAPE), the sounding was capped as indicated by a convective inhibition (CIN) of about 100 J kg^{-1}. Strong 0 to 3 km storm relative helicity (SRH) indicated the support for the development of rotating updrafts during the supercell phase of the storm.

The observed storm was multicellular during its early stage, developing high reflectivities and several dominant updrafts by 2305 (Fig. 5a). At approximately 2330, the storm made a right turn and slowed as it moved southeastward (Fig. 6). Rapid storm growth at all levels is noticed at 2330. The graupel volume of the storm increases in height and amount at a greater rate during this period than at any earlier time (Fig. 7a), while the updraft volume increases from 70 km^3 to 110 km^3 in about 0.5 hour (Fig. 7b). During this period, the Doppler derived maximum updraft speed was near 50 m s^{-1} (Tessendorf and Rutledge 2002) as the storm assumed a supercell structure and intensified and grew in areal coverage. A bounded weak echo region (BWER) also became apparent following the right turn (Fig. 8a-c).

The LMA indicated that the storm began producing lightning at 2150 (Fig. 9a). The lightning rate in the developing stages was 20 flashes per min, but by approximately 0015 the storm reached a maximum of 300 flashes per min (Fig. 9a). During the first three hours, the storm produced on the order of 10,000 total flashes (Table 1). The flash counting algorithm determined an actual "flash" as that consisting of at least 10 source points detected from the LMA's VHF detectors in close proximity and time to remove noise (Wiens et al. 2002). The first cloud-to-ground (CG) flash was detected at 2239 by the National Lightning Detection Network (NLDN). The first ground flash and approximately 90% of the CG flashes thereafter were positive. A total of 140 positive and 19 negative CG flashes were counted by the NLDN during the first three hours of the storm. Both the total flash rate and CG flash rate rapidly increased as the storm displayed extensive development and made a right turn at approximately 2330 (Fig. 9a).

The charge structure from the 29 June storm was inferred using LMA activity and EFMs. Ob-

servations from the LMA can be used to infer charge structure since detected leaders move through regions of opposite polarity charge, the LMA preferentially detects negative polarity breakdown, and inferred charge regions therefore tend to be positive (Hamlin et al., 2003). By the time positive CG flashes occur in the storm, a persistent mid-level positive charge region had developed. Hence, an inverted charge structure was inferred from the LMA observations of positive CG flashes in the present case. The bidirectional ground flashes typically initiated with upward negative leader development into the positive charge region just above 5 km simultaneously with downward positive leader development through a negative charge region to ground. A balloon borne EFM sent through the updraft region of the storm depicted a main positive charge region centered near 9 km and an upper negative charge region centered at 11 km using the 1-D Gauss method of interpretation of Marshall and Rust (1995), as further discussed in Section 3.8.

b. Model initialization

The 29 June supercell storm was simulated on an 80 by 80 by 20 km domain. The horizontal grid spacing was 1 km, while the grid was stretched vertically from 200 m at the surface to 500 m above 12 km. The model environment was determined using a modified version of the NCAR mobile GLASS sounding from Goodland, KS (Fig. 4). The temperature and moisture in the convective boundary layer (CBL) was increased to better depict surface observations of the environment into which the storm moved (Fig. 3). In particular, a mobile mesonet observation near the storm (Fig. 3b) recorded higher temperatures and dewpoints than the Goodland sounding at 2022 (E. Rasmussen, personal communication, 2004). The base of the elevated residual layer capping the moist CBL was warmed adiabatically to maintain a minimum concentrated cap strength, thus controlling the spurious growth of instabilities and preserving the mixed layer. The instability of the environment in the modified sounding was thus greatly increased, raising the CAPE from 1370 $\mathrm{J\,kg^{-1}}$ to 2875 $\mathrm{J\,kg^{-1}}$ and lowering the CIN from 100.3 $\mathrm{J\,kg^{-1}}$ to 22.1 $\mathrm{J\,kg^{-1}}$. The Bulk Richardson Number (BRN), defined as the ratio of the CAPE to the lower tropospheric vertical wind shear, increases from 10.3 to 23.1. The CAPE and BRN of the modified sounding supported possible supercell development (Weisman and Klemp 1982). The model environment was horizontally homogeneous as defined by the modified sounding. A warm bubble ($\Delta\theta = 3\,K$) with randomized thermal perturbations and a radius of 9 km was used to initialize the simulation.

c. Dynamical and microphysical evolution

The present model configuration allows no feedback from the electrification to the microphysics or dynamics. Therefore, each of the four simulations has exactly the same dynamical and microphysical evolution. The simulated storm initially develops an elongated multicell structure (Fig. 5b) with successive main updraft cores along the edge of the outflow on the upshear side. By 76 min, the storm has developed a solid core of reflectivity extending to ground with a deep updraft and forward anvil region. During the first 60 min, the storm moves towards the east-northeast. It is hypothesized that storm rotation and the cold pool have intensified sufficiently to force the storm to turn right towards the southeast and decelerate by 90 min. At 103 min, the precipitation core intensifies as a precipitation-free, cloud-filled mesocyclone develops on the southwest flank (Fig. 5d). By 116 min, the simulated storm has developed a pronounced BWER coincident with the intense main updraft on the southwest flank of the storm (Fig. 8d-f). The storm continues along a southeasterly track for the remainder of the simulation (Fig. 6).

The timing of the right turn is used as a basis for comparison between the simulated and observed storms. The initial development of the observed storm is much slower than in the simulations due to the distinctly different initiation processes, the latter being initialized by a thermal bubble and the former probably forced by a deep boundary layer roll circulation just east of the circulation (e.g., Ziegler et al. 1997). The development of the observed and modeled storms are in rather close agreement from the time of the right turn onward, as supported by comparison of storm morphologies after 90 min of the simulation and 2330 in the observed storm (e.g., Figs. 7 and 8).

The maximum updraft speed of the simulated storm reaches $30\,\mathrm{m\,s^{-1}}$ at 16 min and remains stronger throughout the simulation, with a peak of $61\,\mathrm{m\,s^{-1}}$ at 147 min (Fig. 10). The simulated supercell exhibits evidence of convective surges during its life cycle. The first growth phase occurs at approximately 20 minutes with increases in updraft mass flux (Fig. 10), graupel volume (Fig. 7c), and updraft volume (Fig. 7d). Another convective surge is centered at 80 minutes (Figs. 7c-d, 10) as the storm veers toward its southerly track. The maximum strength of the storm occurs between 140 and 160 min, when updraft mass flux and graupel volume reach peak values and a reflectivity maximum of 69 dBZ is attained. The overall simulated storm evolution is similar to that of the observed storm, especially after 90 min. This agreement is significant as most of the total lightning

and virtually all the CG flashes occur after the right turn in the simulations and the observed storm.

d. Evolution of electrical properties

1). SAUNDERS AND PECK NONINDUCTIVE CHARGING

As previously discussed in Section 2b, the sign of the Saunders and Peck (SP98) noninductive charging is dependent on rime accretion rate (RAR) and the degree of supercooling. The high liquid water content in the updraft caused transfer of positive charge to graupel to dominate the charge produced by the SP98 scheme during the early electrification phase. The resulting charge morphology features a mid-level positive charge with an upper negative charge at 28 min (Fig. 11a).

The inverted dipolar charge structure is replaced by an inverted tripolar structure at about 35 min (not shown), as inductive charging and precipitation recycling and fallout quickly develop a lower negative charge region for the third layer. By 76 min, the storm exhibits an inverted tripole structure with a main mid-level positive charge region between two negative charge regions. All three charges extend horizontally through much of the storm (Fig. 11b). A positive surface corona charge layer is also noted below 0.5 km AGL (all heights above ground level) at this time. The mature stage of the storm at 116 min depicts a very complex structure with opposite charges occurring at the same altitude (Fig. 11c). The reflectivity core regions continue to maintain a tripolar structure, but outside this region there are five or more vertically stacked charge regions. The overall charge structure is similar to that of an inverted storm as proposed by Marshall et al. (1995b) with complexities as described in Stolzenburg et al. (1998).

Simulated intra-cloud (IC) flashes begin at 28 min, with a flash rate of approximately 30 flashes per minute during the first hour (Fig. 9b). The IC flash rate briefly reaches a maximum of 264 flashes per min at 120 min, then decreases slowly while maintaining a flash rate above 150 flashes per min during the remainder of the simulation. Lightning leaders travel preferentially through layers of opposite charge, with positive leaders concentrated in negative charge near 5 km and 13 km (Fig. 12a). Conversely, mid-levels of the storm are dominated by negative leaders and positive charge (Fig. 12b).

The SP98 scheme produces a total of 98 positive ground flashes, the first occurring at 67 min, with no negative ground flashes produced (Table 1). The CG flashes typically initiate between

5 and 7 km, between the main positive charge region above and a negative charge region below (Fig. 13). In the simulation, positive CG flashes are composed of a negative leader traveling upward through positive charge and a positive leader traveling downward through negative charge to ground (Fig. 13). Most simulated lightning flashes exhibit considerable branching by lightning leaders in all directions from the point of initiation. On occasion, a leader might may go directly to ground, though often a flash goes to ground more than 1 km away (horizontally) from its initiation point. The direction of the path of leaders to ground is dependent on the distribution of charge surrounding the leader as it develops. The majority of the CG strikes is located just downshear of the main convective core, though some occur directly under the main updraft.

2). RIMING RATE NONINDUCTIVE CHARGING

The riming rate (RR) noninductive charging scheme is also dependent on the rime accretion rate, though with a different critical RAR than the SP98 scheme. This produces a slightly different profile of charge distribution but with many results similar to those of SP98. During early electrification, the electrical structure of the main core is comprised of a short-lived inverted dipole with a lower positive charge and upper negative charge in the main cell due to positive noninductive charging to graupel (Fig. 11d). At 76 min, the storm develops an inverted tripole extending horizontally beyond the main core (Fig. 11e). By the time the storm reaches its mature stage, near 116 min, the charge profile has become quite complex (Fig. 11f). As in the SP98 simulation, the overall charge structure in the main cores continue to consist of an inverted tripole, while other areas of the storm exhibit a much more complex structure.

The first IC flashes begin at 28 min in the simulation (Fig. 9c). For the remainder of the first 60 min, the flash rate averages roughly 15–20 flashes per min. A maximum flash rate of 252 per min is reached at 128 min and the average flash rate during the third hour is approximately 170 per min. The upper region of the storm (10 to 18 km) is dominated by positive leaders while the mid-levels (5 to 12 km) is dominated by negative leaders (Fig. 12c,d). The lowest third of the storm (2 to 6 km) is dominated by positive leaders.

A total of 128 simulated positive CGs are produced (Table 1), the first occurring at 77 min into the simulation (Fig. 9c), and no negative ground flashes are produced. Nearly all of the CG flashes initiate between 4 and 8 km. Within the storm, the majority of flashes reach ground downshear of

the main convective core. Though lagging the SP98 simulation in total flashes, the RR charging scheme produces more ground flashes throughout the simulation. However, the simulated positive CGs in the RR simulation are morphologically similar to positive CGs in the SP98 simulation.

3). TAKAHASHI NONINDUCTIVE CHARGING

The charge structure developed with the Takahashi (TAKA) noninductive charging scheme is similar to the conceptual model of a normal polarity dipole or tripole structure. During early electrification, a normal dipole charge structure develops in the updraft region (Fig. 11g). The storm quickly develops a normal tripole structure as a lower positive charge region is formed. At 76 min, the charge structure consists of a mid-level negative charge, an upper positive charge region, and a lower positive charge region situated in the updraft area (Fig. 11h). By 116 min, the storm is reaching its mature stage and the charge structure is much more complex (Fig. 11i). Normal tripoles are evident in the reflectivity cores, though outside of these convective cores the charge structure contains up to six vertically stacked charge regions.

IC flashes begin at 27 min and a flash rate averages about 20 flashes per min for the first hour (Fig. 9d). Steady growth of the flash rate continues for the second hour, and a maximum of 208 flashes per min occurs at 122 min. A drop off in flash rate follows, and during the third hour the flash rate stays near 120 flashes per min. Positive leaders are concentrated in the mid-levels of the storm between 4 and 10 km (Fig. 12e). Although the majority of negative leaders are in the upper levels of the storm between 8 and 16 km, negative leaders are also noted in lower portions of the storm (Fig. 12f).

A total of 63 ground flashes are produced during the TAKA simulation (Table 1). All CGs produced are negative, the first occurring at 71 min (Fig. 9d). The initiation points for ground flashes are limited to between 4 and 6 km, between a lower positive charge region and middle negative region.

4). GARDINER-ZIEGLER (GZ) NONINDUCTIVE CHARGING

The Gardiner-Ziegler (GZ) noninductive scheme develops a normal dipolar or tripolar charge structure that is broadly similar to the TAKA simulated charge distribution. However, the lower positive charge region in the GZ simulation is weaker than the lower positive charge region in the

TAKA simulation during the maturing phase of development. Early electrification is dominated by collisions within the updraft region at temperatures less than the reversal temperature. At 28 min, the charge structure is a normal dipole with a main negative charge region and an upper positive charge region (Fig. 11j). As the storm develops at 76 min, upper positive and middle negative regions are maintained in the precipitation core with a weak lower positive charge beginning to form (Fig. 11k). At 116 min, there is a normal tripole structure within the updraft regions. However, pockets of charge create a complex structure for the majority of the storm (Fig. 11l).

The first IC flashes in the GZ simulation occur at 28 min (Fig. 9e). The flash rate increases rapidly, averages near 40 flashes per min for the first hour, and noticeably exceeds the early flash rates of the other NI parameterizations. The maximum flash rate occurs at 126 min where a peak of 264 flashes per min is reached. The GZ scheme subsequently maintains a higher flash rate for longer than any of the other schemes, nearly 200 flashes per min for the next hour. Negative leaders are concentrated within the upper half of the storm between 8 and 16 km (Fig. 12h). A few negative leaders also occur episodically in the lowest portions of the storm around 120 min, and again after 140 min. The lower half of the storm (2 to 10 km) contains mostly positive leaders (Fig. 12g).

Though the GZ scheme generates frequent IC flashes, it produces only 5 CG flashes during the entire simulation, 3 positive and 2 negative (Table 1). Hence, the charges produced by GZ are not as effectively lowered as in the other parameterizations. The lack of a strong tripolar charge structure of the storm is significant, since the 3 positive CG initiations occur along the boundary between the upper positive and main negative charge regions located around 11 km AGL. The first two ground flashes are positive and initiate near 120 min at 12 and 11 km respectively. The third is also positive initiating at 160 min, at 13 km AGL, and downshear from the main convective area of the storm. The height of the positive CG initiations for the GZ simulation is anamalous for any model simulation, possibly implying an unrealistic result of the CG lightning scheme since the length of the positive and negative leaders in the three flashes are significantly unbalanced. The first negative CG occurs at 170 min initiating from 4.2 km from underneath the main updraft. The final negative CG of the simulation occurs just before 180 min and is initiated just below 6 km. Both negative CGs seem more realistic and broadly comparable to the negative CGs produced by the TAKA scheme.

e. Observed and simulated electric field meter soundings

A balloon carrying an electric field meter (EFM) was released from Brewster, KS at 0004 UTC into the updraft region of the storm (Fig. 8 a,c). Using a 1-D Gauss model (Marshall and Rust 1991; Stolzenburg and Marshall 1994), it is assumed that vertical gradients in E_z are caused by the EFM rising through regions of charge. Interpreting the observed vertical electric field profile using the 1-D Gauss technique, the 29 June storm's charge profile is inferred to consist of a main positive charge region from 8 to 10 km and a main negative charge region from 10 to 11 km (Fig. 14f). A detailed analysis of the three dimensional electric field vector profile reveals additional smaller charge regions along the balloon track through the reflectivity core of the storm (MacGorman et al. 2005).

A simulated EFM was also "released" into the main updraft of each of the model simulations at 113 min (Figs. 8d,f and 14b). The simulated EFM followed roughly the same track at approximately the same time during the storm's life cycle as the observed EFM sounding. Both the simulated and observed soundings are contained within the intense main updraft region, rising through the BWER into the overlying precipitation core. Consequently, almost all charge is above 8 km at the level where the EFM penetrates the top of the BWER. The soundings maintain similar tracks below 12 km. The simulated EFM sounding detrains from storm top above 12 km, while the observed sounding moves horizontally and subsequently descends through the storm without reaching the top (possibly due to the balloon being punctured by hail). The observed and simulated temperature and relative humidity with respect to water saturation display remarkably similar profiles below 12 km.

An inverted tripole charge structure is observed in the simulated balloon sounding during the SP98 and RR simulations (Fig. 14a,c). The height and magnitude of the upper negative and main positive charge regions are similar to those of the corresponding regions from the observed storm. Both simulations also include a small lower negative charge region near 8 km, a feature that is not revealed in the observed sounding. The simulated sounding could be closer to the lower negative charge region than the observed sounding, the latter beginning further away from the storm (eg., Figs. 8c, f and 14b).

The EFM soundings from the TAKA and GZ simulations depict a normal tripolar charge structure (Fig. 14d,e), in direct opposition to the inverted tripole of the SP98 and RR simulations

(Fig. 14a,c). The TAKA and GZ soundings reveal a small lower positive charge region below 8 km, a main negative charge region centered near 10 km, and an upper positive charge region from 10 to 12 km.

The analysis of the downward EFM profile from 29 June depicts a much more complex profile in the precipitation core downwind from the updraft region (MacGorman et al. 2005). Interpretation of charges via the 1D Gauss model depicts four or five levels of charge in the precipitation core, in contrast with two or three charge layers in the main updraft region. A similar profile is also obtained in the SP98 simulation outside the main updraft regions (eg. Fig. 11c), where pockets of charge account for added complexity to the profile.

4. Discussion

a. Role of noninductive charging in charge structure development

An examination of the hydrometeor charging at 76 min illustrates the impact of the various laboratory charging constraints on the simulated electrification. The majority of collisions between riming graupel and ice occurs in the main updraft region. The graupel in the cloudy updraft is charging positively at all temperatures by the SP98 scheme due to the high rime accretion rates (Fig. 15a). Immediately adjacent to the updraft, graupel is charging negatively owing to the very low rime accretion rates. These negatively charged graupel are subsequently transported via sedimentation and advection to lower regions of the storm (Fig. 15a). The SP98 scheme provides positive charging to graupel at rime accretion rates above $1\,\mathrm{g\,m^{-2}s^{-1}}$ at higher temperatures and above $3\,\mathrm{g\,m^{-2}s^{-1}}$ at lower temperatures (Fig. 2a). Thus, the inverted polarity charge structure is controlled by the positive noninductive charging to graupel in the updraft region, which provides the main positive charge center for the storm. The upper negative charge region is due in part to the negative charge transfer to ice from rebounding collisions with the graupel in the updraft. The lower negative charge region subsequently develops as a combination of negative noninductive charging outside the main updraft core, inductive charging, and precipitation fallout and recycling.

The RR and SP98 parameterizations have slightly different functional dependencies of charging on rime accretion rate, although the two charging schemes produce very similar charge distributions. At 76 min, the main difference in graupel charging between RR and SP98 occurs adjacent to

the updraft from -30°C to -40°C (Fig. 15b), where the SP98 $RAR_{\rm crit}$ drops toward zero (Fig. 2b). Thus, in this region the graupel is charging positively in the SP98 simulation and charging negatively in the RR simulation. The resultant charge structure for the RR simulation is very similar to the SP98 simulation. However, the lower negative charge region in the RR simulation is stronger and slightly more dominant than in the SP98 simulation, probably influenced by the additional negatively charged graupel recycling through lower levels of the storm.

The TAKA noninductive scheme produces a charge structure almost exactly opposite the SP98 and RR charging schemes. Instead of a dependence on rime accretion rate, the controlling variable for the Takahashi scheme is cloud liquid water content. At 76 min, the graupel is charging negatively in the updraft region, which contains liquid water contents from 0.5 to 2.5 g m^{-3} at temperatures less than -10°C (Fig. 15c). The predominately negative charging of graupel within the updraft region controls the polarity (Fig. 2c), producing a main negative charge region. An upper positive charge region develops from positive noninductive charge transfer to snow and ice, which are lofted higher than the graupel due to the differential fallspeeds of the hydrometeors. A small lower positive charge region develops from weak positive noninductive charge transfer to graupel outside the main updraft core in low liquid water content. This lower positive charge region is also enhanced by inductive charging of roughly the same maginitude as noninductive charging.

At 76 min, the GZ noninductive charging scheme develops a charge structure consistent with a normal dipole. The main negative charge region is attributable to the graupel gaining negative charge at temperatures less than -15°C (Fig. 2d) as well as precipitation fallout (Fig. 15d). The upper positive charge region develops as a result of the ice gaining positive charge from collisions with graupel and advection of the ice through the upper part of the storm. Small pockets of weak positive charge form at lower levels due to positive noninductive charge transfer to graupel at temperatures greater than -15°C (Fig. 15d). The GZ scheme possibly has difficulty producing the lowest charge region due to the temperature-only dependence inherent in the scheme. While the other schemes produce opposite-sign charging in the downshear updraft flank, the GZ scheme only produces opposite charging at the base of the updraft, which is then countered by charging at lower temperatures higher within the updraft. Inductive charging acts to enhance the preexisting charge outside of the updraft core.

The overall charge structure of the mature storm in all the simulations is much more complex

than the basic dipole or tripole model, in agreement with the results of Stolzenburg et al. (1998). The early storm development is multicellular, and each successive updraft and precipitation core produces another area of charging. Thus, pockets of concentrated charge develop throughout the storm. The charge structure is further complicated by the parameterized lightning activity. When a simulated leader travels through a region of opposite polarity, a localized reversal in the net charge can occur within the larger charge region leading to a more complex charge structure (Helsdon et al. 1992; Mansell et al. 2002; Coleman et al. 2003). Also, layers of charge are advected on cloud ice through the anvil region due to the bulk effects of essentially continuous lightning with either IC or CG branching (Ziegler and MacGorman 1994).

b. Positive CG development relative to storm polarity

The simulations produce similar total flash counts to the approximately 10,000 flashes observed over three hours in the 29 June 2000 storm (Table 1). The observed storm produces predominately positive CG flashes, as do the simulations employing the SP98 and RR noninductive charging schemes. In both the observed and simulated storms (i.e., SP98, RR, TAKA), cloud-to-ground flashes account for roughly one percent of the total lightning activity.

As previously discussed in Section 3, the LMA measurements and EFM soundings indicate that the observed storm develops an inverted polarity charge structure by the beginning of positive CG activity. Only the SP98 and RR simulations develop an inverted polarity charge structure, while the TAKA and GZ simulations develop normal polarity charge structures dominated by a main negative charge region. The prevailing polarity of the simulated ground flashes is governed by the polarity of the main mid-level charge region in the storm.

The development of a lower negative region in the SP98 and RR simulations and in the observed storm is crucial for positive CG development. In both the simulations and the observed storm, almost all of the positive CG flashes initiate at approximately 6 km, approximately the boundary of the main positive charge region and the lower negative charge region. This notion is analogous to the hypothesis of Williams et al. (1989) that negative CG flashes require a preexisting lower positive charge region. Mansell et al. (2002) generalized this relationship, noting that positive (negative) ground flashes developed only after formation of a lower negative (positive) charge region in simulated storms. In the present simulations, negative CG flashes are produced only

where the lowest charge layer is positive, as noted in results from the TAKA noninductive charging scheme. During the GZ simulation, positive CG flashes occur earlier in the storm when the lowest charge layer is negative. Negative CG flashes begin later, once a lower positive charge region develops. The SP98 and RR charging schemes maintain a lower negative charge region for most of the simulated storm's lifetime, thus producing only positive ground flashes.

The step-leader model of Mazur and Ruhnke (1993), a basis for the Mansell et al. (2002) lightning parameterization, suggests that lightning is initiated between propagates bidirectionally through opposite polarity charge regions. The simulated positive CGs develop following the Mazur-Ruhnke model, with negative leaders traveling upward and branching through the main positive charge region and positive leaders traveling downward through the smaller lower negative charge region to ground (e.g., Fig. 13). Each flash is initiated where the electric field is approximately maximized between positive and negative charge regions (Fig. 13). The positive channel follows areas of negative charge that have descended toward ground. The descent of charge to ground appears to be a prerequisite for all simulated ground flashes, facilitating flash propagation through regions of weak electric potential due to local field enhancement at the leader tip. The RAR-based simulation results are consistent with the Hamlin et al. (2003) analysis of LMA data (Fig. 16). The LMA analysis depicts the initiation and development of positive CGs and the corresponding inferred net charge. The Hamlin et al. (2003) analysis points to the importance of the polarity of the lowest charge region for the polarity of the ground flashes.

Other hypotheses concerning the required charge structure for storms with predominately positive polarity ground flashes have been discussed by Williams (2001) and Lang and Rutledge (2002). These include a tilted dipole (i.e., the updraft is sheared by strong mid- and upper-level winds, exposing the upper positive charge region to ground), an elevated charging mechanism, precipitation unshielding (i.e., the positive region is exposed to ground), and an inverted dipole, none of the latter being consistent with the present observations and model results. Instead, the latter results suggest that an inverted tripolar charge structure is the necessary condition for predominately positive ground flashes in the 29 June storm. Neither the tilted dipole nor the elevated charging mechanism are consistent with predominately positive CG activity initiated at the lower levels of the storm between the main positive and lower negative charge regions. As discussed in Mansell et al. (2002), precipitation unshielding is an unlikely mechanism for positive CG activity, since a negative layer

would still be required to initiate the lightning. The inverted dipole is insufficient for a comprehensive description of the total charge structure, since the lower negative charge layer seems to be a necessary condition for positive CGs and since the overall charge structure is much more complex than two layers of charge.

c. Positive CG production relative to storm microphysics and kinematics

The microphysics and kinematics of the storm play major concerted roles in establishing the storm charge structure and lightning polarity. The polarity of charge deposited on hydrometeors is dependent on liquid water content and other microphysical properties via the NI charging parameterizations. Similarly, the NI charging rate is controlled by the rebounding collision rate of graupel, which depends on the strength and size of the updraft region. All the simulations have the same microphysical characteristics (e.g., liquid water and ice particle contents). Therefore, the polarity of the simulated ground flashes is modulated chiefly by the particular noninductive charging scheme used and the resultant charge structure. Though approaching adiabatic values, the simulated maximum liquid water content remains too low to support a change from predominately negative charging of graupel to positive charging in the updraft region using the TAKA noninductive charging scheme as recently hypothesized by Carey et al. (2003) and Lang and Rutledge (2002). Instead, the TAKA simulation maintains a normal polarity charge structure through the simulation, thus resulting only in negative CG activity. Lang and Rutledge (2002) suggested that one of the factors leading to predominately positive CG flashes in several mid-latitude storms (one of which is 29 June) is a large updraft volume relative to other storms. The simulated and observed storms contain a storm total updraft volume consistently greater than 300 km^3 through the $-10^{\circ}\mathrm{C}$ level (Fig. 7b,d). The large mixed-phase updraft volumes produce a high rate of graupel-ice and hail-ice collisons, resulting in higher total and ground flash rates independent of ground flash polarity.

The observations depict the tendency for positive CG flashes to cluster downwind of the main updraft region, and this is mirrored by the SP98 and RR simulations (e.g., Fig. 17). The clustering of positive CGs downwind of the main updraft may be caused by the presence of descending graupel and hail in that region. In the observed storm, the correlation between regions of hail and positive CG activity could be due to positive charge residing within the radar-inferred hail

echo region (K. C. Wiens, personal communication, 2004). As positively charged graupel and hail advect and sediment out of the main updraft region, cloud-to-ground lightning would initiate between the main graupel and hail core containing positive charge and a lower region of negatively charged hydrometeors. MacGorman and Burgess (1994) and Stolzenburg (1994) found that a large percentage of predominately positive CG activity occurred with storms in which large hail was reported. Carey et al. (2003) found that the positive CG activity tended to cluster in the area of highest reflectivity during the 1998 Spencer, SD supercell, though no large hail was reported with this storm. During the 29 June storm, almost all of the positive CGs were colocated with hail echos (Wiens et al. 2003). The simulations suggest a degree of correlation between the timing of melting graupel and the onset of positive CG flashes in lower regions of the storm (Fig. 18a,b), though trends of graupel volume clearly follow increasing positive CG rates. Although hail content is highly correlated with graupel content in the simulations, hail carries relatively little charge compared to graupel. A key reason for development of positive CG flashes may be the descent of the lower negative charge from the inverted tripole on graupel, hail, and meltwater rain, thus carrying negative charge through the lowest regions of the storm.

Carey et al. (2003) found that the positive CG rate increased during or just after pulses in storm growth during the Spencer storm. Similar relationships are suggested during the SP and RR simulations, though it is difficult to determine a direct relationship. The peak positive CG rates of 3-5 per min occur shortly after the maximum graupel volume is reached at 150 min (Fig. 18a). The mass flux, updraft volume and updraft speed also achieve short-lived maximum values around 150 min (Fig. 18c-e). CG activity does not begin until the onset of rainfall, as inferred from the rain mass time series (Fig. 18b).

d. Total flash rate relative to storm microphysics and kinematics

The total flash rate is perhaps the best electrical representation of the overall microphysical activity and intensity of the storm. Graupel volume demonstrates a high degree of correlation with total lightning activity in both the simulations (Fig. 19) and the observed storm. Suggestions of pulsing activity in total flash rate occur at different periods of the storm. With increasing graupel volume (Fig. 19), updraft mass flux (Fig. 18c), or updraft volume (Fig. 18d), the collisions occurring between graupel and ice particles also increase. Consequently, noninductive charging and

electrification increase, forcing the flash rate to increase to control the maximum electric field.

High visual correspondences between the various series shown thus far are strongly influenced by the continuous growth of the storm during the three hours of the simulation. After linearly detrending the time series of each parameter and total flash rate (e.g., MacGorman et al. 1989), an unbiased cross-correlation estimate reveals a strong relationship between the variables (Table 2). Graupel volume and total lightning show a strong correlation at approximately zero time lag, while updraft mass flux and updraft volume suggest a maximum correlation preceding total lightning by about 10 min. It is apparent in both the model simulations and the observed storm that the total flash rate closely models storm intensity. Thus, total flash rate is perhaps the best electrical representation of the evolving size and severity of the observed and simulated 29 June STEPS supercell storm.

5. Conclusions

Though dipole and tripole electrical structures are useful conceptual models, both observations and model simulations typically show that the charge structures of actual storms are much more complex. Rarely, if ever, does a uniform charge density of a given polarity extend horizontally through the entire extent of the storm. On the contrary, the charge density at a given height often varies widely within a storm and can even reverse polarity multiple times. However, the main updraft and precipitation core region of the 29 June storm is approximated by an inverted tripole with an upper positive screening layer.

Simulated and observed lightning flashes have very similar morphological characteristics and statistical variability. In both the LMA observations and the model simulations, normal-polarity cloud flashes initiate below positive charge and above negative charge, while inverted-polarity flashes initiate below negative charge and above positive charge. In all cases in which positive ground flash initiation could be observed in sufficient detail in the LMA data, it appeared that initiation occurred in the convective core only when the lowest charge was negative, as was the case in the simulations. The occurrence of ground flashes in the simulations appeared to be associated with charge descending into very low regions of the storm, possibly corresponding to descending precipitation cores as reported by MacGorman et al. (1989) and Carey and Rutledge (1996). However, accurately diagnosing the location and timing of ground flash activity is problematic. The

stochastic nature of lightning initiation and propagation, at least in the model, prevents knowledge of where a particular flash will propagate or even whether one that does initiate in a favorable region will reach ground.

As suggested by several observational studies (Lhermitte and Krehbiel 1979), the total flash rate of the storm simulations was positively correlated with fluctuations in the intensity of convection and precipitation. These correlations are forced by the noninductive charging and the subsequent three-dimensional motions of the charged hydrometeors. Observational studies and the simulations both show that the total flash rate, instead of ground flash rate or storm polarity, provides the best electrical diagnostic of the microphysical and kinematic intensity of a storm.

The simulated storm charge structure is dependent on which noninductive charging parameterization is used. The two schemes based on rime accretion rate (SP98 and RR) develop very similar inverted polarity charge distributions that can be described roughly as inverted polarity tripoles. The liquid water content scheme (TAKA) and the simpler temperature reversal scheme (GZ) develop normal polarity charge distributions. The rime accretion rate parameterizations appear to provide the best overall agreement with electrical observations from 29 June. However, it also develops inverted polarity charge distributions in a range of other environments in other storm simulations (not shown), many of which actually produce normal polarity charge distributions, suggesting that the riming rate parameterizations do not universally apply. Thus, it is speculated that perhaps the magnitude and polarity of charge produced by the noninductive mechanism is affected by an additional parameter(s) not yet included in the laboratory experiments used as the basis for conventional noninductive charging parameterizations.

Acknowledgements

We thank Kyle Wiens and Sarah Tessendorf for providing LMA flash counts, multiple radar analyses, and results including graupel volume and updraft volume from the 29 June storm. We also thank Erik Rasmussen for providing mobile mesonet observations for the 29 June case. Support for this research was provided under National Science Foundation grant ATM-0119398. Additional funding for this research was provided under NOAA-OU Cooperative Agreement NA17RJ1227.

References

Baker, H. B., H. J. Christian, and J. Latham, 1995: A computational study of the relationships linking lightning frequency and other thundercloud parameters. *Quart. J. Roy. Meteor. Soc.*, **99**, 10627–10632.

Branick, M. L. and C. A. Doswell, III, 1992: An observation of the relationship between supercell structure and lightning ground strike polarity. *Wea. Forecasting*, **7**, 143–149.

Brooks, I. M. and C. P. R. Saunders, 1994: An experimental investigation of the inductive mechanism of thunderstorm electrification. *J. Geophys. Res.*, **99**, 10627–10632.

Carey, L. D., W. A. Peterson, and S. A. Rutledge, 2003: Evolution of cloud-to-ground lightning and storm structure in the Spencer, South Dakota, tornadic supercell of 30 May 1998. *Mon. Wea. Rev.*, **131**, 1811–1831.

Carey, L. D. and S. A. Rutledge, 1996: A multiparameter radar case study of the microphysical and kinematic evolution of a lightning producing storm. *J. Meteor. and Atmos. Phys.*, **59**, 33–64.

— 1998: Electrical and multiparameter radar observations of a severe hailstorm. *J. Geophys. Res.*, **103**, 13979–14000.

Carpenter, R. L., K. K. Droegemeier, and A. M. Blyth, 1998: Entrainment and detrainment in numerically simulated cumulus congestus clouds. Part I: General results. *J. Atmos. Sci.*, **55**, 3417–3432.

Coleman, L. M., T. C. Marshall, M. Stolzenburg, T. Hamlin, P. R. Krehbiel, W. Rison, and R. J. Thomas, 2003: Effects of charge and electrostatic potential on lightning propogation. *J. Geophys. Res.*, **108**, doi:10.1029/2002JD002718.

Gardiner, B., D. Lamb, R. L. Pitter, J. Hallett, and C. P. R. Saunders, 1985: Measurements of initial potential gradient and particle charges in a montana summer thunderstorm. *J. Geophys. Res.*, **90**, 6079–6086.

Gish, O. H., 1944: Evaluation and interpretation of the columnar resistance of the atmosphere. *Terr. Magn. Atmos. Electr.*, **49**, 159–168.

Hamlin, T., P. R. Krehbiel, R. J. Thomas, W. Rison, and J. Harlin, 2003: Electrical structure and storm severity inferred by 3-D lightning mapping observations during STEPS. *Proceedings, 12th Int. Conf. on Atmospheric Electricity*, ICAE, Versailles, France, 189–192.

Helsdon, J. H., Jr. and R. D. Farley, 1987: A numerical modeling study of a montana thunderstorm: 2. model results versus observations involving electrical aspects. *J. Geophys. Res.*, **92**, 5661–5675.

Helsdon, J. H., Jr., W. A. Wojcik, and R. D. Farley, 2001: An examination of thunderstorm-charging mechanisms using a two-dimensional storm electrification model. *J. Geophys. Res.*, **106**, 1165–1192.

Helsdon, J. H., Jr., G. Wu, and R. D. Farley, 1992: An intracloud lightning parameterization scheme for a storm electrification model. *J. Geophys. Res.*, **97**, 5865–5884.

Jayaratne, E. R., 1993: The heat balance of a riming graupel pellet and the charge separation during ice-ice collisions. *J. Atmos. Sci.*, **50**, 3185–3193.

Jayaratne, E. R., C. P. R. Saunders, and J. Hallett, 1983: Laboratory studies of the charging of soft hail during ice crystal interactions. *Quart. J. Roy. Meteor. Soc.*, **109**, 609–630.

Johns, R. A. and C. A. Doswell, III, 1992: Severe local storms forecasting. *Wea. Forecasting*, **7**, 588–612.

Keith, W. D. and C. P. R. Saunders, 1990: Further laboratory studies of the charging of graupel during ice crystal interactions. *Atmos. Res.*, **25**, 445–464.

Klemp, J. B. and R. B. Wilhelmson, 1978: Simulations of right- and left-moving storms produced through storm splitting. *J. Atmos. Sci.*, **35**, 1097–1110.

Krehbiel, P. R., R. J. Thomas, W. Rison, T. Hamlin, J. Harlin, and M. Davis, 2000: GPS-based mapping system reveals lightning inside storms. *Eos, Trans. Amer. Geophys. Union*, **81**, 21–32.

Lang, T. J. and S. A. Rutledge, 2002: Relationships between convective storm kinematics, precipitation, and lightning. *Mon. Wea. Rev.*, **130**, 2492–2506.

Lhermitte, R. and P. R. Krehbiel, 1979: Doppler radar and radio observations of thunderstorms. *IEEE Trans. on Geoscience Electron.*, **GE-17**, 162–171.

MacGorman, D. R. and D. W. Burgess, 1994: Positive cloud-to-ground lightning in tornadic storms and hailstorms. *Mon. Wea. Rev.*, **122**, 1671–1697.

MacGorman, D. R., D. W. Burgess, V. Mazur, W. D. Rust, W. L. Taylor, and B. C. Johnson, 1989: Lightning rates relative to tornadic storm evolution on 22 May 1981. *J. Atmos. Sci.*, **46**, 221–250.

MacGorman, D. R. and W. D. Rust, 1998: *The electrical nature of storms*. Oxford University Press, 422 pp.

MacGorman, D. R., W. D. Rust, P. R. Krehbiel, E. C. Bruning, and K. C. Wiens, 2005: The electrical structure of two supercell storms during STEPS. *Mon. Wea. Rev.*, **133**, in press.

Mansell, E. R., 2000: *Electrification and lightning in simulated supercell and nonsupercell thunderstorms*. Ph.D. thesis, University of Oklahoma, Norman, OK.

Mansell, E. R., D. MacGorman, C. L. Ziegler, and J. M. Straka, 2002: Simulated three-dimensional branched lightning in a numerical thunderstorm model. *J. Geophys. Res.*, **107**, doi:10.1029/2000JD000244.

Mansell, E. R., D. R. MacGorman, C. L. Ziegler, and J. M. Straka, 2005: Charge structure and lightning sensitivity in a simulated multicell thunderstorm. *J. Geophys. Res.*, **1**, [in press].

Marshall, T. C., M. P. McCarthy, and W. D. Rust, 1995a: Electric field magnitudes and lightning initiation in thunderstorms. *J. Geophys. Res.*, **100**, 7097–7103.

Marshall, T. C., W. Rison, W. D. Rust, M. Stolzenburg, J. C. Willett, and W. P. Winn, 1995b: Rocket and balloon observations of electric field in two thunderstorms. *J. Geophys. Res.*, **100**, 20815–20828.

Marshall, T. C. and W. D. Rust, 1991: Electric field soundings through thunderstorms. *J. Geophys. Res.*, **96**, 22297–22306.

Mazur, V. and L. Ruhnke, 1993: Common physical processes in natural and artificially triggered lightning. *J. Geophys. Res.*, **98**, 913–930.

Mitzeva, R. and C. P. R. Saunders, 1990: Thunderstorm charging: Calculations of the effect of ice crystal size and graupel velocity. *J. Atmos. Terr. Phys.*, **52**, 241–245.

Pereyra, R. G., E. E. Avila, N. E. Castellano, and C. Saunders, 2000: A laboratory study of graupel charging. *J. Geophys. Res.*, **105**, 20803–20812.

Perez, A. H., L. J. Wicker, and R. E. Orville, 1997: Characteristics of cloud-to-ground lightning associated with violent tornadoes. *Wea. Forecasting*, **12**, 428–437.

Reynolds, S. E., M. Brook, and M. F. Gourley, 1957: Thunderstorm charge separation. *J. Meteor.*, **14**, 426–436.

Rison, W., R. J. Thomas, P. R. Krehbiel, T. Hamlin, and J. Harlin, 1999: A GPS-based three-dimensional lightning mapping system: Initial observations in central New Mexico. *Geophys. Res. Lett.*, **26**, 3373–3576.

Rust, W. D., D. R. MacGorman, and R. T. Arnold, 1981: Positive cloud-to-ground lightning flashes in severe storms. *Geophys. Res. Lett.*, **8**, 791–794.

Rust, W. D. and T. C. Marshall, 1996: On abandoning the thunderstorm tripole-charge paradigm. *J. Geophys. Res.*, **101**, 23499–23504.

Saunders, C. P. R. and S. L. Peck, 1998: Laboratory studies of the influence of the rime accretion rate on charge transfer during crystal/graupel collisions. *J. Geophys. Res.*, **103**, 13949–13956.

Seimon, A., 1993: Anomalous cloud-to-ground lightning in an F5-tornado-producing supercelll thunderstorms on 28 August 1990. *Bull. Amer. Meteor. Soc.*, **74**, 189–203.

Solomon, R. and M. Baker, 1998: Lightning flash rate and ttype in convective storms. *J. Geophys. Res.*, **103**, 14079–14096.

Stolzenburg, M., 1994: Observations of high ground flash densities of positive lightning in summertime thunderstorms. *Mon. Wea. Rev.*, **122**, 1740–1750.

Stolzenburg, M. and T. C. Marshall, 1994: Testing models of thunderstorm charge distribution with Coulomb's law. *J. Geophys. Res.*, **99**, 25921–25932.

Stolzenburg, M., W. D. Rust, and T. C. Marshall, 1998: Electrical structure in thunderstorm convective regions 3. Synthesis. *J. Geophys. Res.*, **103**, 14097–14108.

Straka, J. M., 1989: *Hail Growth in a Highly Glaciated Central High Plains Multi-cellular Hailstorm*. Ph.D. thesis, University of Wisconsin-Madison, Dept. of Meteorology, Madison, WI, 53706.

Straka, J. M. and E. R. Mansell, 2005: A bulk microphysics parameterization with multiple ice precipitation categories. *J. Appl. Meteor.*, **44**, 445–466.

Takahashi, T., 1978: Riming electrification as a charge generation mechanism in thunderstorms. *J. Atmos. Sci.*, **35**, 1536–1548.

— 1983: Numerical simulation of winter cumulus electrification. Part I: Shallow cloud. *J. Atmos. Sci.*, **40**, 1257–1280.

— 1984: Thunderstorm electrification – a numerical study. *J. Atmos. Sci.*, **41**, 2541–2558.

Tessendorf, S. A., L. J. Miller, K. C. Wiens, and S. A. Rutledge, 2005: The 29 June 2000 supercell observed during STEPS. Part I: Kinematics and microphysics. *In review at J. Atmos. Sci.*.

Tessendorf, S. A. and S. A. Rutledge, 2002: Kinematic and microphysical evolution of the 29 June supercell during STEPS. *Preprints, 21st Conf. on Severe Local Storms*, Amer. Meteor. Soc., San Antonio, TX, 307–310.

Vonnegut, B., 1963: Some facts and speculations concerning the origin and role of thunderderstorm electricity. *Meteorolog. Monogr.*, **5**, 224–241.

Weisman, M. L. and J. B. Klemp, 1982: The dependence of numerically simulated convective storms on vertical wind shear and buoyancy. *Mon. Wea. Rev.*, **110**, 504–520.

Wiens, K. C., S. A. Tessendorf, and S. A. Rutledge, 2002: June 29 STEPS supercell storm: Relationships between kinematics, microphysics, and lightning. *Preprints, 21st Conf. on Severe Local Storms*, Amer. Meteor. Soc., San Antonio, TX, 315–318.

— 2003: STEPS June 29, 2000 Supercell: Observations of kinematic, microphysical, and electrical structure. *Proceedings, 12th Int. Conf. on Atmospheric Electricity*, ICAE, Versailles, France, 263–266.

Williams, E. R., 2001: The electrification of severe storms, Severe Convective Storms. *Meteor. Monogr.*, C. A. Doswell, III, ed., Amer. Meteor. Soc., volume 50, 527–561.

Williams, E. R., M. E. Weber, and R. E. Orville, 1989: The relationship between lightning type and convective state of thunderclouds. *J. Geophys. Res.*, **94**, 213–220.

Winn, W. P., C. B. Moore, C. R. Holmes, and L. G. Byerley, III, 1978: A thunderstorm of July 16, 1975, over Langmuir Laboratory: A case study. *J. Geophys. Res.*, **83**, 3080–3092.

Wojcik, W. A., 1994: *An Examination of Thunderstorm Charging Mechanisms Using the IAS 2D Storm Electrification Model*. Master's thesis, So. Dakota Schl. Mines Technol., Rapid City, SD.

Ziegler, C. L., T. J. Lee, and R. A. Pielke, Sr., 1997: Convective initiation at the dryline: a modeling study. *Mon. Wea. Rev.*, **125**, 1001–1026.

Ziegler, C. L. and D. R. MacGorman, 1994: Observed lightning morphology relative to modeled space charge and electric field distributions in a tornadic storm. *J. Atmos. Sci.*, **51**, 833–851.

Ziegler, C. L., D. R. MacGorman, J. E. Dye, and P. S. Ray, 1991: A model evaluation of non-inductive graupel-ice charging in the early electrification of a mountain thunderstorm. *J. Geophys. Res.*, **96**, 12833–12855.

Ziegler, C. L., P. S. Ray, and D. R. MacGorman, 1986: Relations of kinematics, microphysics and electrification in an isolated mountain thunderstorm. *J. Atmos. Sci.*, **43**, 2098–2114.

List of Figures

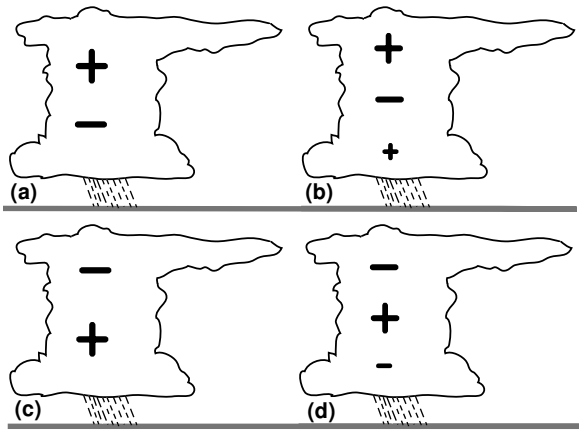

Figure 1: Conceptual model of charge structure of a thunderstorm. (a) Normal dipole model, containing upper positive and lower negative charge centers. (b) Normal tripole model, containing upper positive, main negative, and smaller lower positive charge centers. (c) Inverted dipole, lower positive charge and upper negative charge centers. (d) Inverted tripole, main positive with upper and lower negative charge centers.

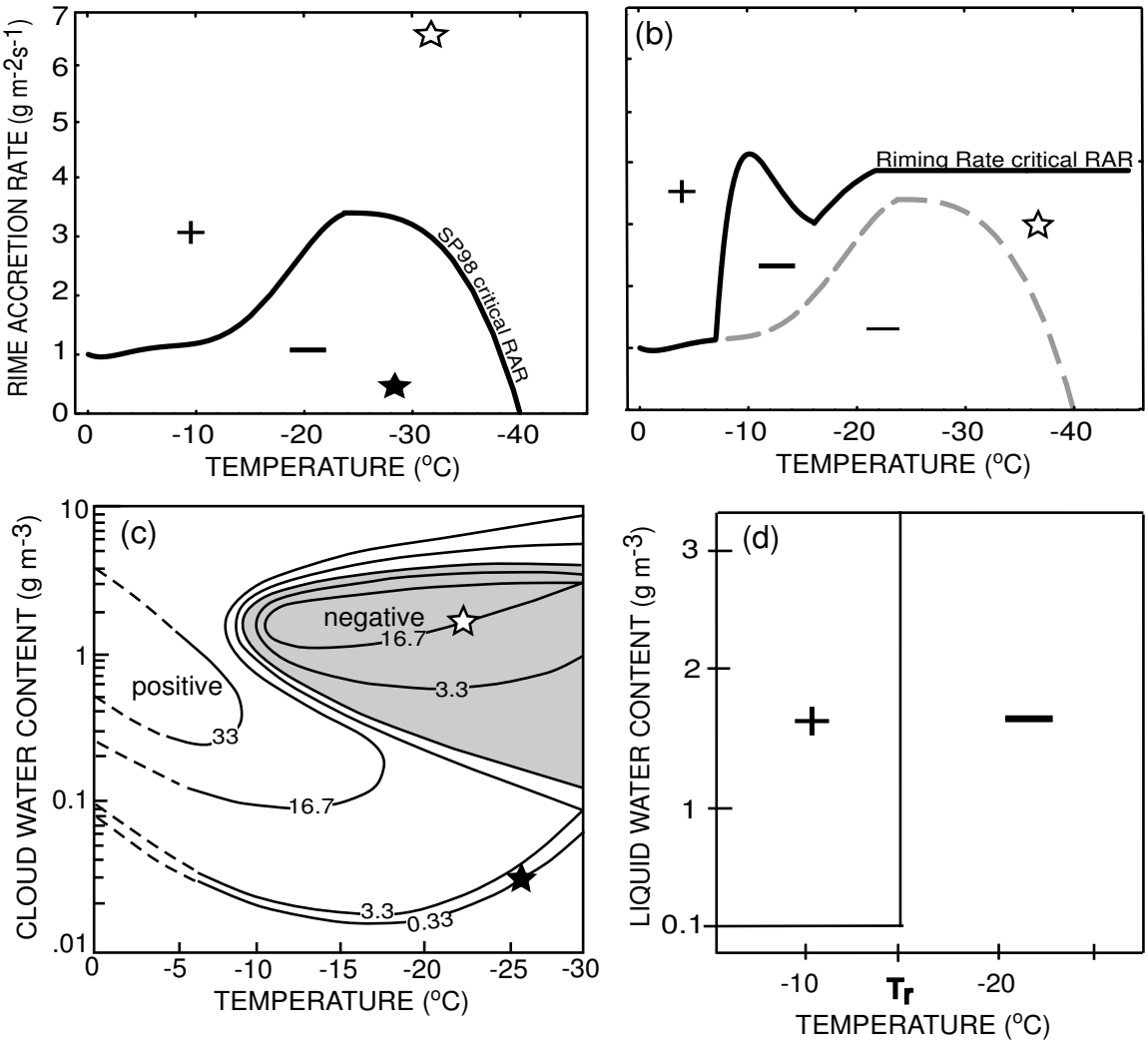

Figure 2: (a) The polarity of charge gained by graupel as a function of temperature and RAR according to the laboratory experiments of Saunders and Peck (1978). Graupel gains positive charge above the curve at higher rime accretion rates and negative charge below the curve. White and black stars correspond to same level of RAR and temperature shown in Fig. 15a. (b) The polarity of charge gained by the graupel as a function of temperature and RAR according to the RR scheme and the SP98 scheme. White star points out difference in positive vs negative charging between RR and SP98 in Fig. 15b at 76 min. (c) The polarity of charge gained by graupel as a function of temperature and cloud water content, adapted from Takahashi (1978). White and black stars correspond to the same level of liquid water content and temperature shown in Fig. 15c. (d) Polarity of the charge gained by graupel during GZ simulation as a function of the reversal temperature and liquid water content.

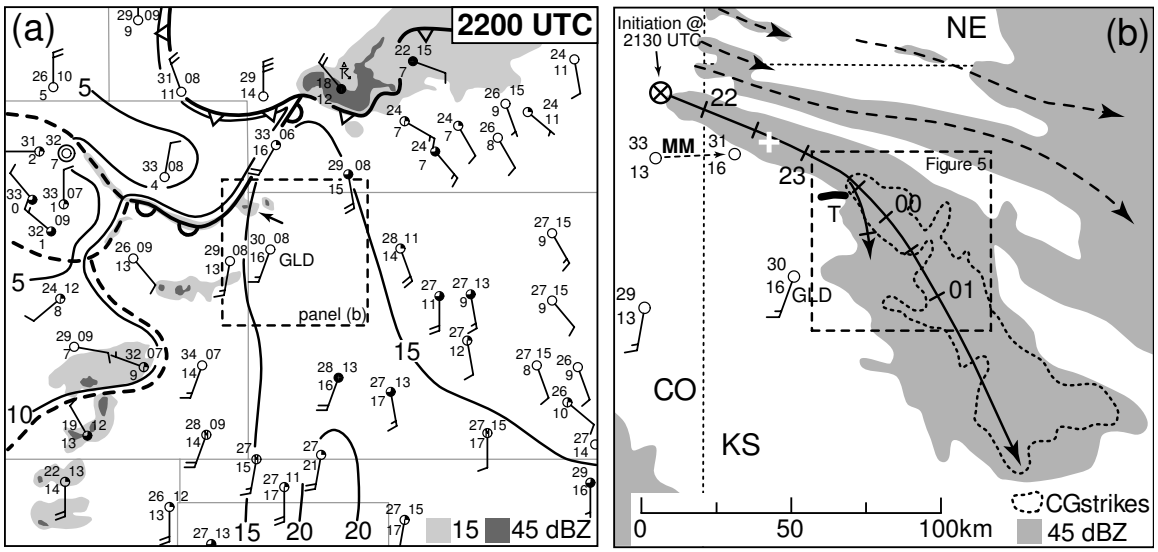

Figure 3: (a) Surface observations and reflectivity over central plains approximately one half hour after the 29 June supercell storm first appeared on radar. A southward moving mesoscale cold front is indicated by the heavy curve with open triangles, a dryline is denoted by the scalloped curve and other mesoscale boundaries indicated by the dashed lines. Isodrosotherms are analyzed every 5°C in grey. The first radar echoes of the storm are denoted by the arrow with in the box for panel (b). (b) Time evolution of storm. 45 dbZ reflectivity swath and NLDN lightning during the period 2100-0300 UTC. Surface observations from Goodland, KS (GLD) and mobile mesonet (MM) at approximately 2200 UTC. The storm path is indicated by the solid line through grey dashed box (see Fig. 6), other storm paths indicated by dashed lines. Panel (b) adapted from Fig. 5 of Tessendorf et al. (2005).

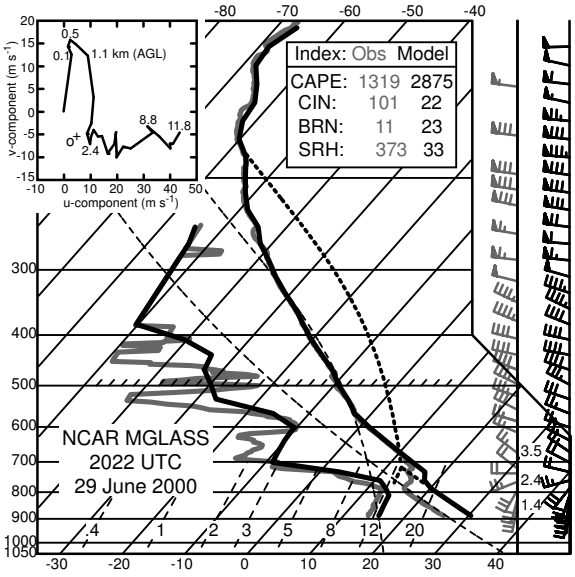

Figure 4: Observed NCAR mobile GLASS sounding released from Goodland, KS at 2022 UTC on 29 June 2000 (thick grey lines). The modified sounding used for model initialization is overlaid (black). The hodograph is the same for both soundings, with corresponding heights (km) AGL denoted. The motion of the observed and modeled storms after developing supercell characteristics is denoted by a plus and a circle respectively. CAPE (J kg^{-1}), CIN (J kg^{-1}), BRN, and 0 to 3 km SRH (m^2 s^{-2}) are shown for both soundings, observed (grey) and modified (black).

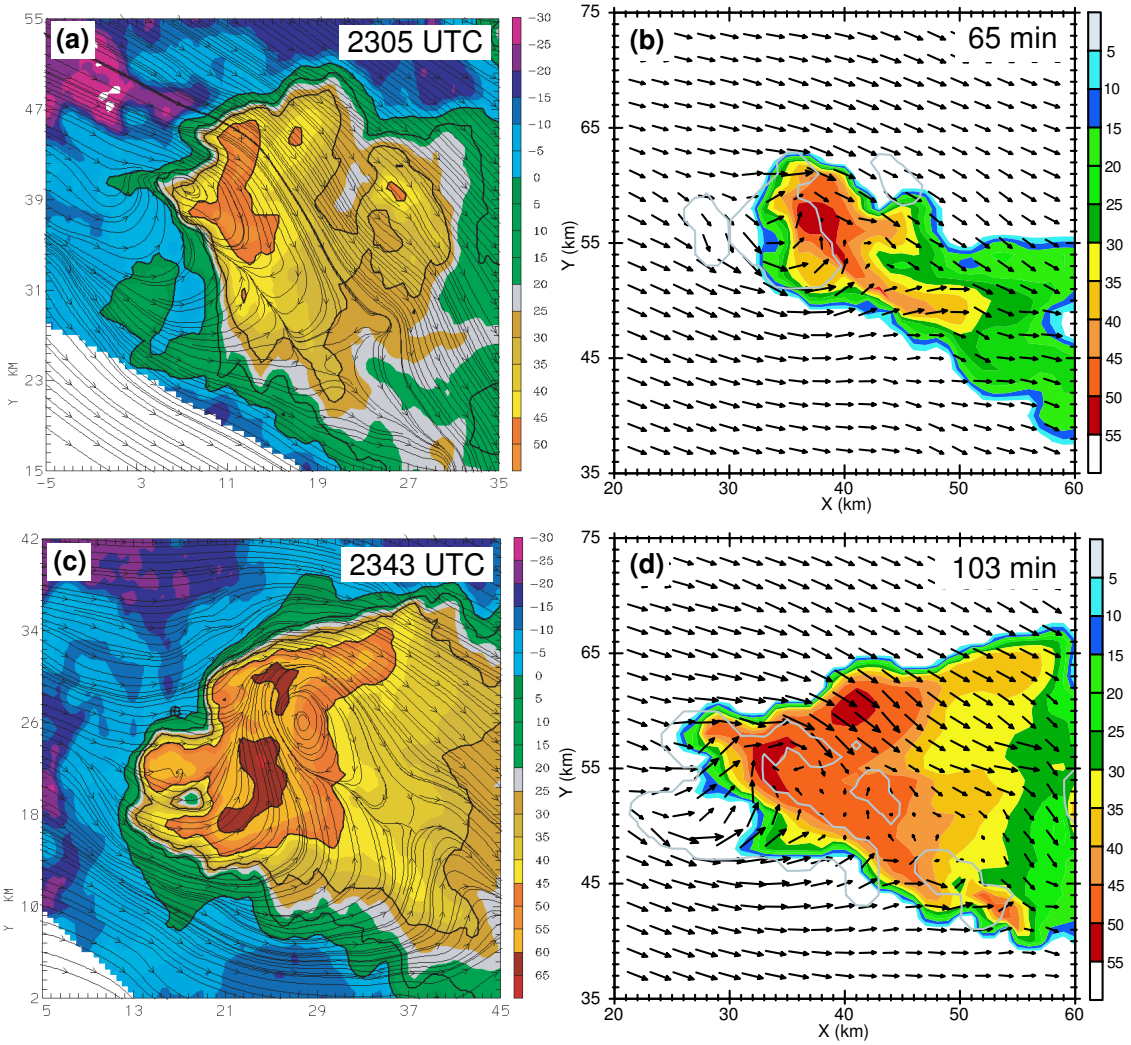

Figure 5: (Left Column) 5 km MSL radar reflectivity from S-Pol with ground relative streamlines overlaid at (a) 2305 UTC (c) 2343 UTC, courtesy S. A. Tessendorf. (Right Column) 4 km AGL (approx. 5 km MSL) parameterized reflectivity from model simulations at (b) 65 min (d) 103 min with ground relative wind vectors and cloud outline (grey) at 4 km (approx. 5 km MSL). Corresponding times are relative to the right turn taken by the observed storm at 2330 UTC and the simulated storm at 90 min (Fig. 6).

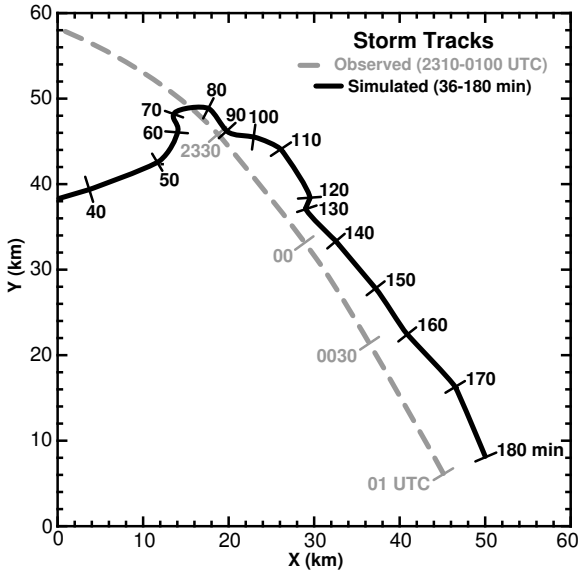

Figure 6: Comparison of the observed and simulated 29 June storm paths in the sub-domain indicated by the dashed box in Fig. 3b. The position of the simulated storm (black curve) is shown every 10 min starting at 36 min after initiation, while the observed storm path (grey dash curve) is indicated from 2310 UTC through 0100 UTC. Observed and simulated storm track positions are assumed to coincide at the 90 min–2330 UTC, corresponding to the right turn.

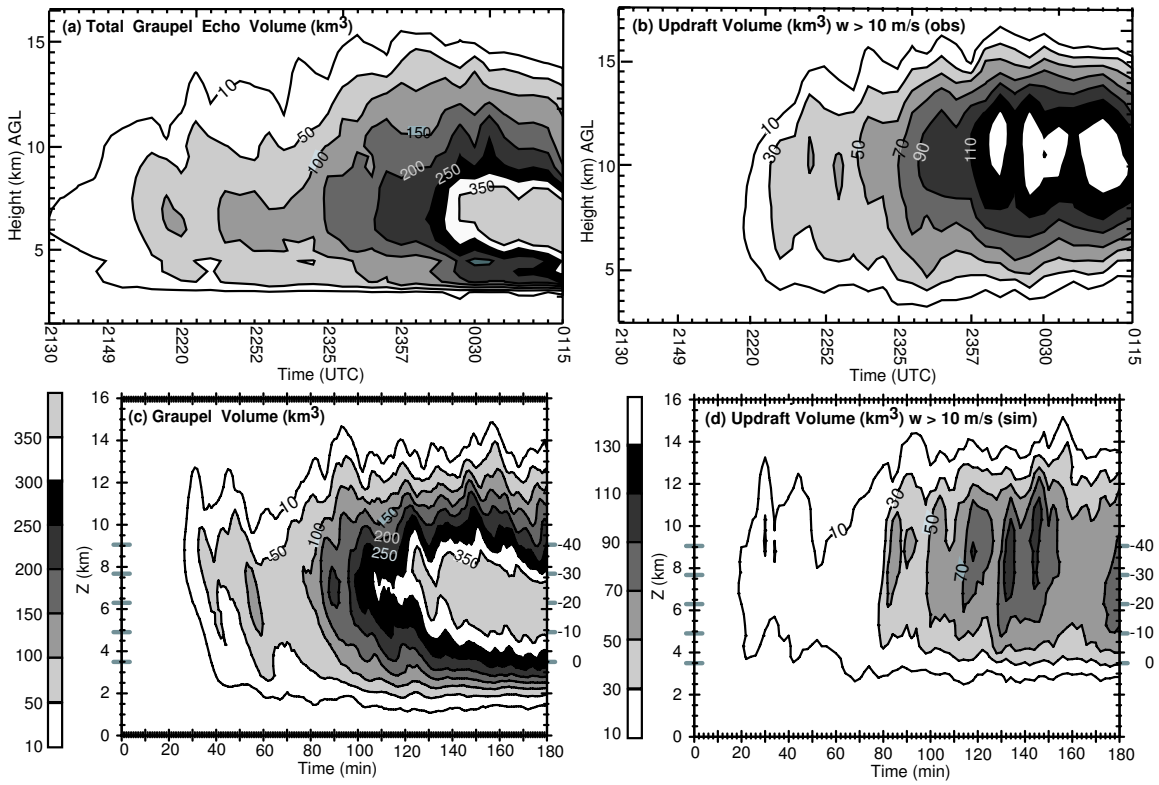

Figure 7: Time-height sections of selected storm variables. (a) Graupel echo volume as inferred from S-Pol radar from 29 June (from K. C. Wiens and S. A. Tessendorf, personal communication, 2004). (b) Updaft volume as inferred from S-Pol radar from 29 June (from K. C. Wiens and S. A. Tessendorf, personal communication). (c) Graupel volume in the simulated storm (km^3). (d) Updraft volume for updrafts $> 10\ m\,s^{-1}$ in the simulated storm (km^3). Same scales are used in panels (a)-(c) and (b)-(d), and the time scale is aligned according to when each storm took its right turn.

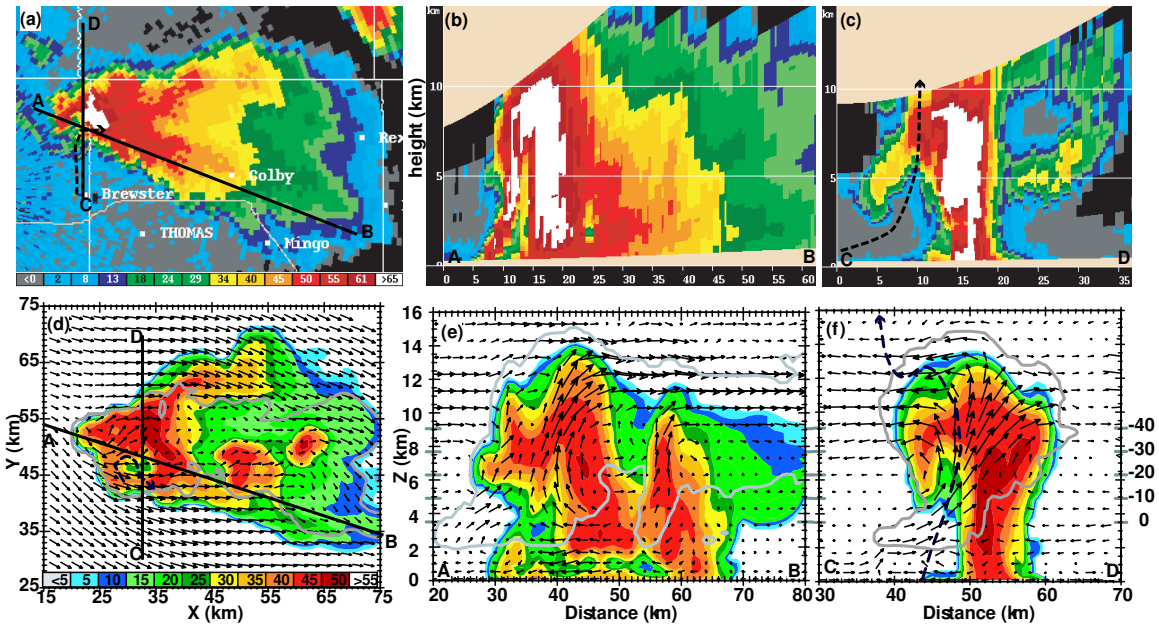

Figure 8: Top row: Radar reflectivity from Goodland, KS WSR 88D radar at 0004 UTC. (a) 0.5° elevation scan, cross-sections for (b) and (c) denoted by solid black lines. The path of the EFM balloon launched from Brewster, KS at approximately 0004 UTC into the main updraft (see Fig. 14) is denoted by a black dashed line. (b) Cross-section along line AB. (c) Cross-section along line CD, path of balloon shown by black dashed line. Bottom row: Reflectivity, ground relative vectors, and cloud outline (grey) from simulations at 116 min. (d) X-Y planar view at 6.8 km. Path of EFM balloon along red line from 0 to 12 km (see Fig. 14). (e) Cross-section along line AB. (f) Cross-section along line CD, maximum vector of 54.5 m s^{-1} in updraft. Path of simulated EFM balloon along red dashed line beginning at 113 min. At 116 min, EFM is just below 2 km. Compare with Fig. 2 of MacGorman et al. (2005).

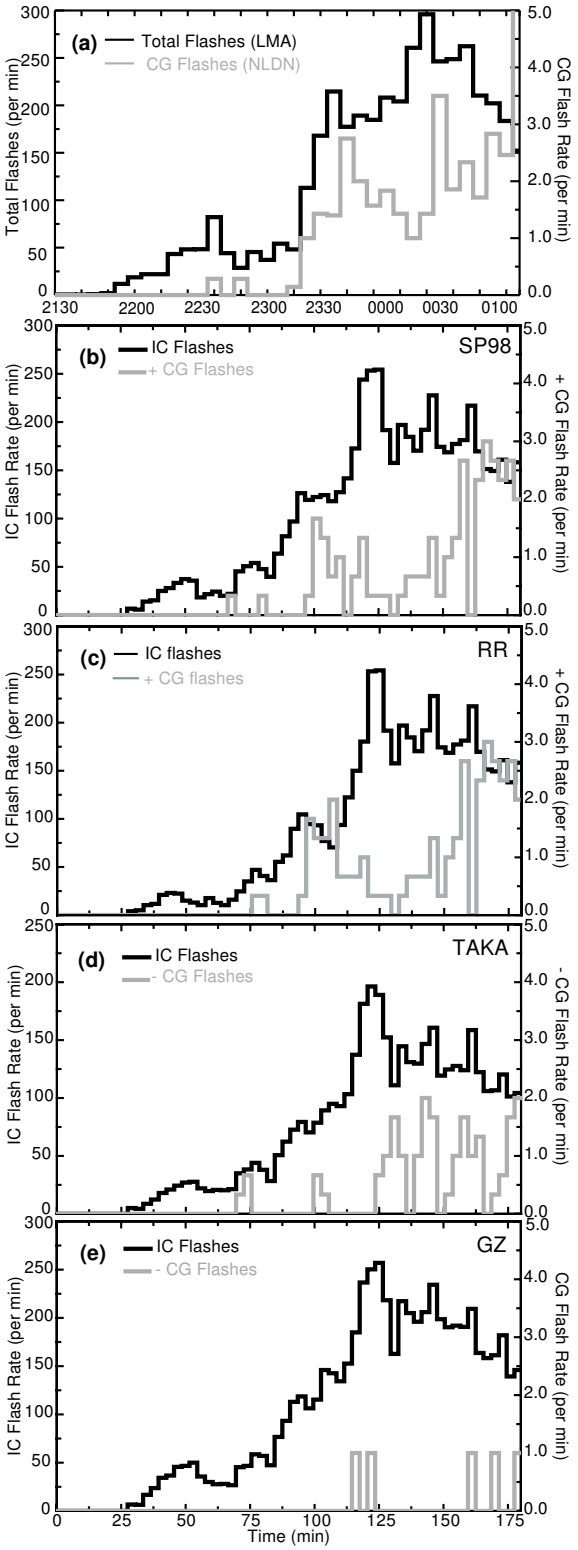

Figure 9: Lightning time series for the 29 June supercell and simulations. (a) Flashes per min counted from LMA detection (black) and total CG per min from NLDN (grey). Adapted from Wiens et al. (2003). (b-e) In-cloud flashes per min (black) and cloud-to-ground flashes per min (grey). (b) SP98 noninductive charging (c) RR noninductive charging (d) TAKA noninductive charging (e) GZ noninductive charging

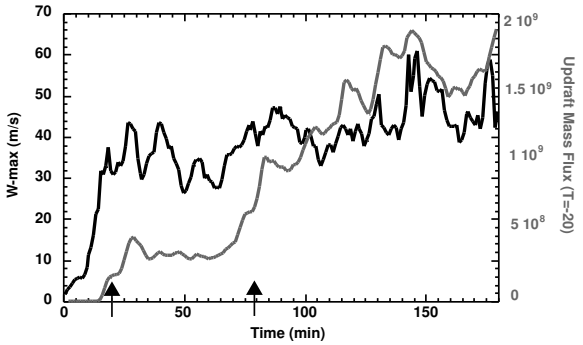

Figure 10: Maximum updraft speed ($\mathrm{m\,s^{-1}}$) (black) and updraft mass flux ($\mathrm{m^3}$) through $T = -20°\mathrm{C}$ (grey) in the simulated 29 June supercell storm Arrows point out periods of rapid intensification.

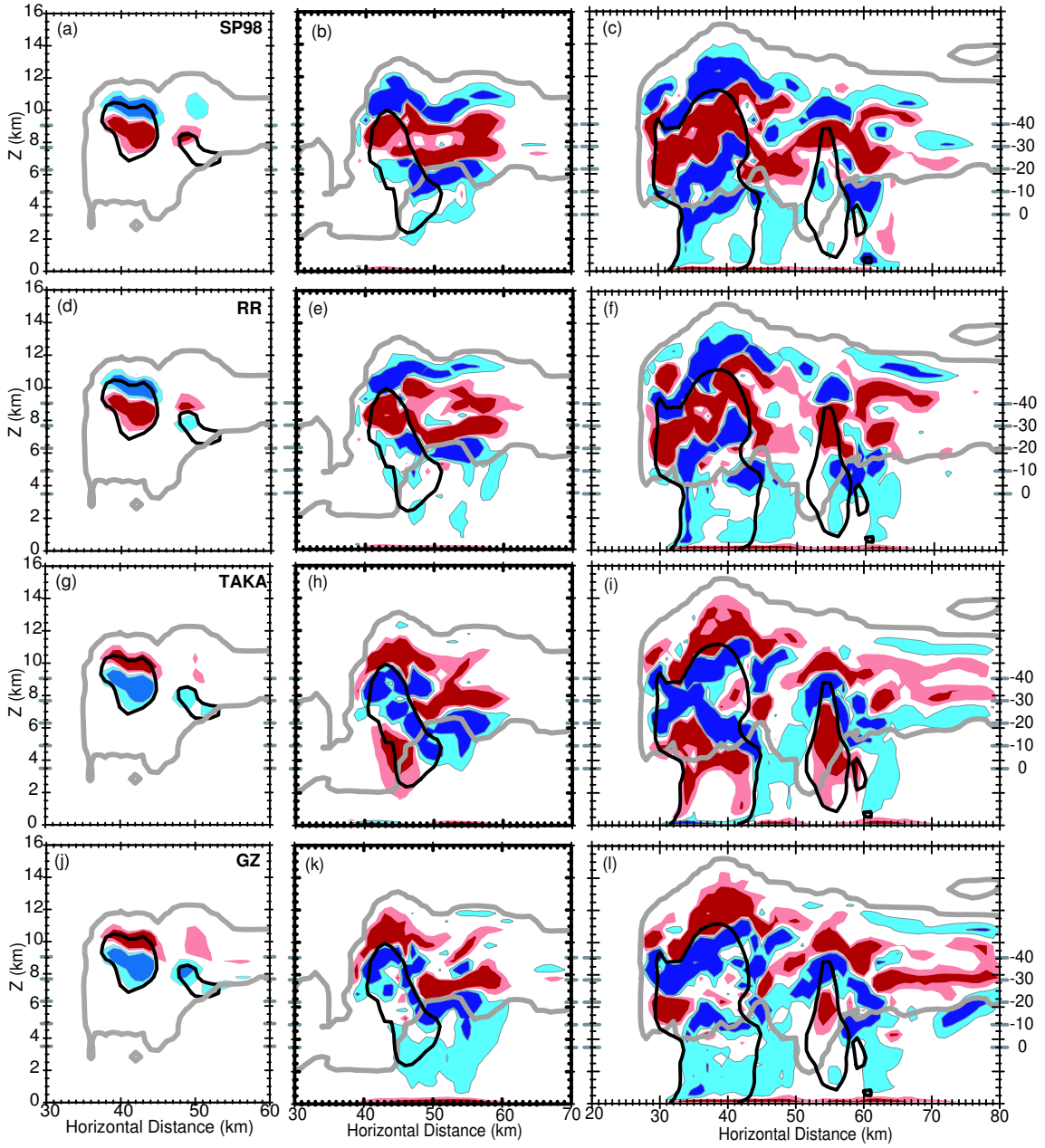

Figure 11: Charge structure for SP98 (a-c), RR (d-f), TAKA (g-i), and GZ (j-l) simulations at 28 min (a, d, g, j), 76 min (b, e, h, k), and 116 min (c, f, i, l). Red and blue shading denotes positive and negative charge regions, respectively. Lighter shading indicates areas of at least + or − 0.1 nC m^{-3}, darker shading indicates areas of at least + or − 0.25 nC m^{-3}. Cloud outline is a grey contour. Black contour is 25 dbz (a,d) and 45 dbz (b,c,e,f). Compare panels (c), (f), (i), and (l) with descent sounding illustrated in panels (a) and (f) of MacGorman et al. (2005).

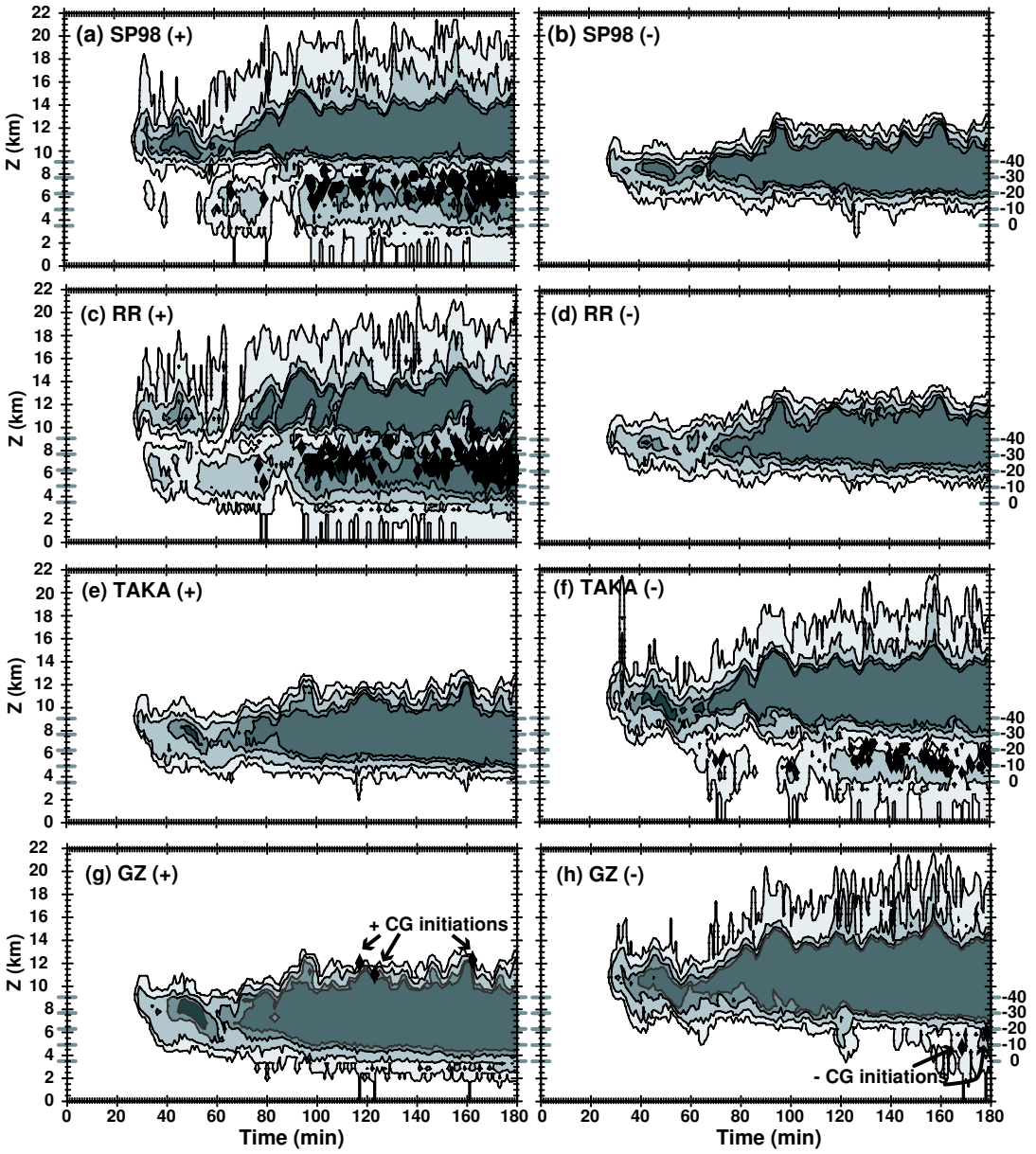

Figure 12: Time-height plots of leader segment density, CG initiation points in solid black fill. (a) SP98 positive leaders, (b) SP98 negative leaders, (c) RR positive leaders, (d) RR negative leaders, (e) TAKA positive leaders, (f) TAKA negative leaders, (g) GZ positive leaders, (h) RR negative leaders.

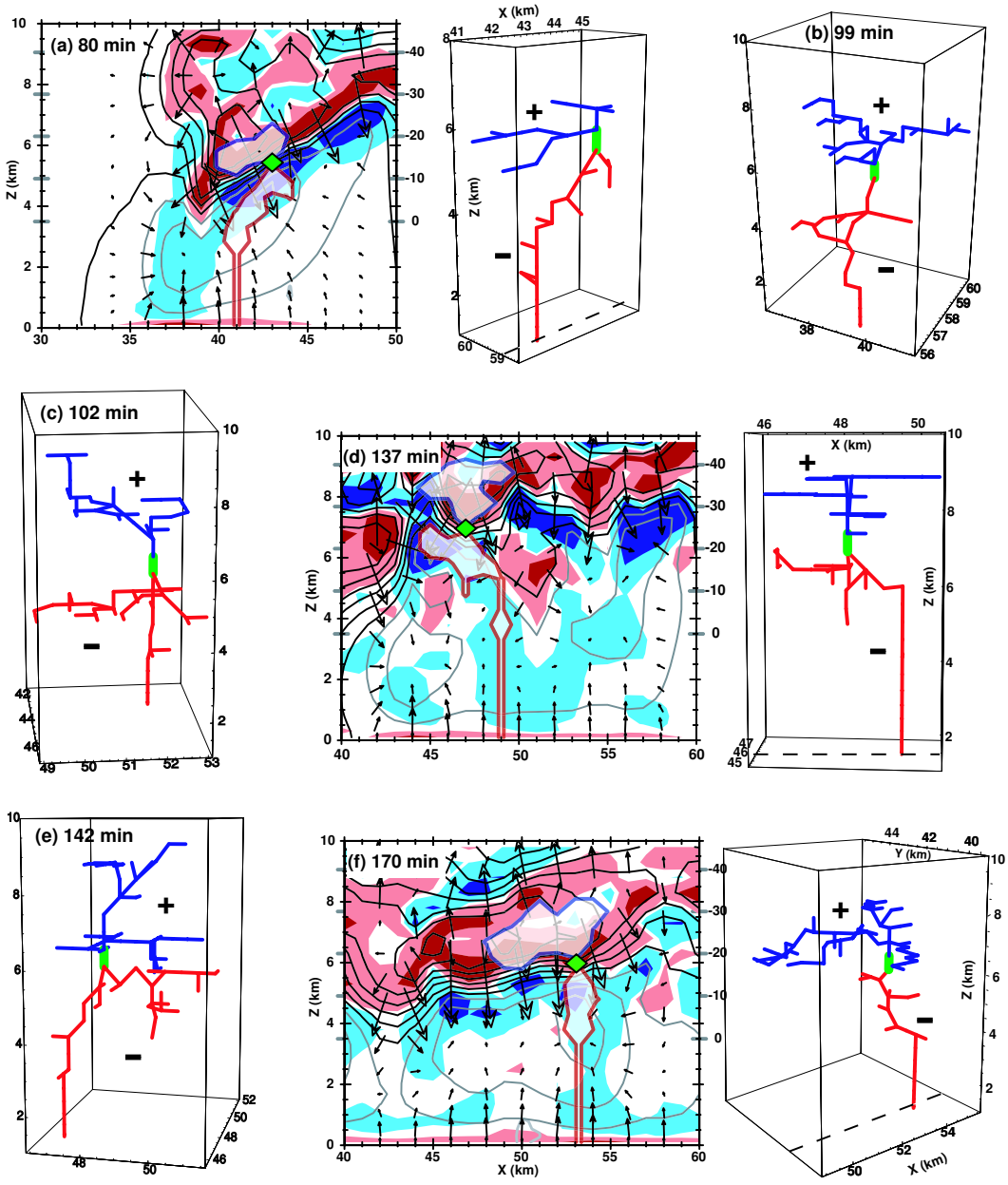

Figure 13: Positive cloud-to-ground flashes during the SP98 simulation. (a) 80 min, Left: Vertical cross-section through storm. Positive and negative charge regions are contoured in solid red and blue respectively, vectors are of the electric field, black and grey contours indicate equipotential lines. Lightning leaders in white fill contour, positive with red outline, negative with blue outline. Right: 3-D view of flash, initiation shown in green, positive leaders in red and negative leaders in blue. Location of x-z cross-section shown in left panel denoted by grey-dashed line. Signs of net charge are indicated. (b) 3-D view of flash at 99 min. (c) 3-D view of flash at 102 min. (d) same as (a), but at 137 min. (e) 3-D view of flash at 142 min. (f) 170 min, values same as (a).

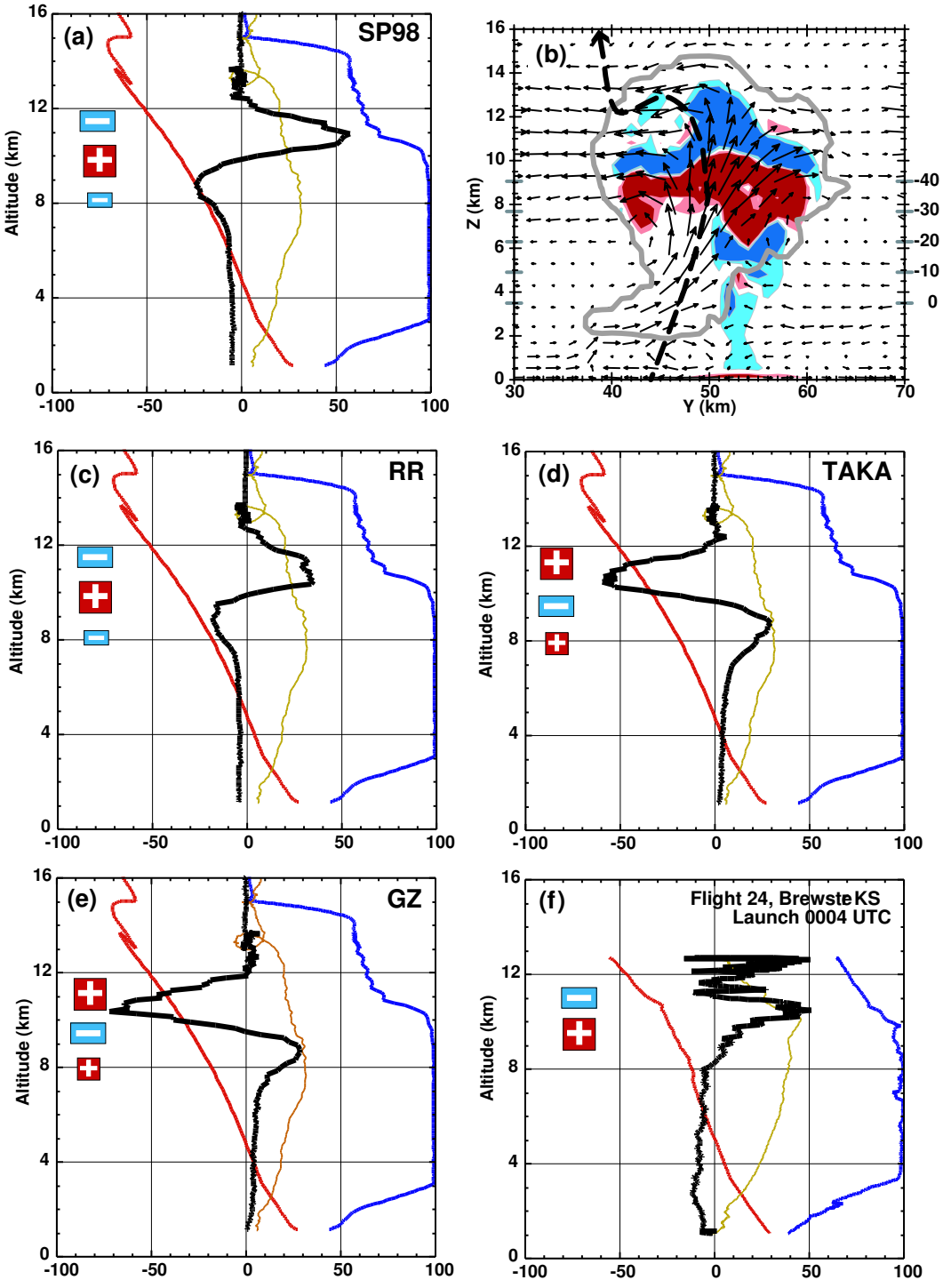

Figure 14: (a, c-e) Simulated EFM at 113 min – 140 min in the 4 different simulations. Graphs show E_z (black), temperature (red), relative humidity (blue), and rise rate of the balloon (brown). Red bars and blue bars represent height of positive and negative charge levels using 1-D approximation to Gauss's Law, smaller bars represent charge region of smaller magnitude. (Height is converted to MSL to compare with obsevations). Flight path of balloon superimposed on reflectivity in Fig. 8d, f. (b) Path of balloon through SP98 simulation denoted by dashed black line, positive (red) and negative (blue) charge regions shown (height AGL). (e) EFM balloon sounding at 00:04:58 – 00:34:09 UTC on 30 June 2000. Same variables as (a). See Fig. 8a, c.

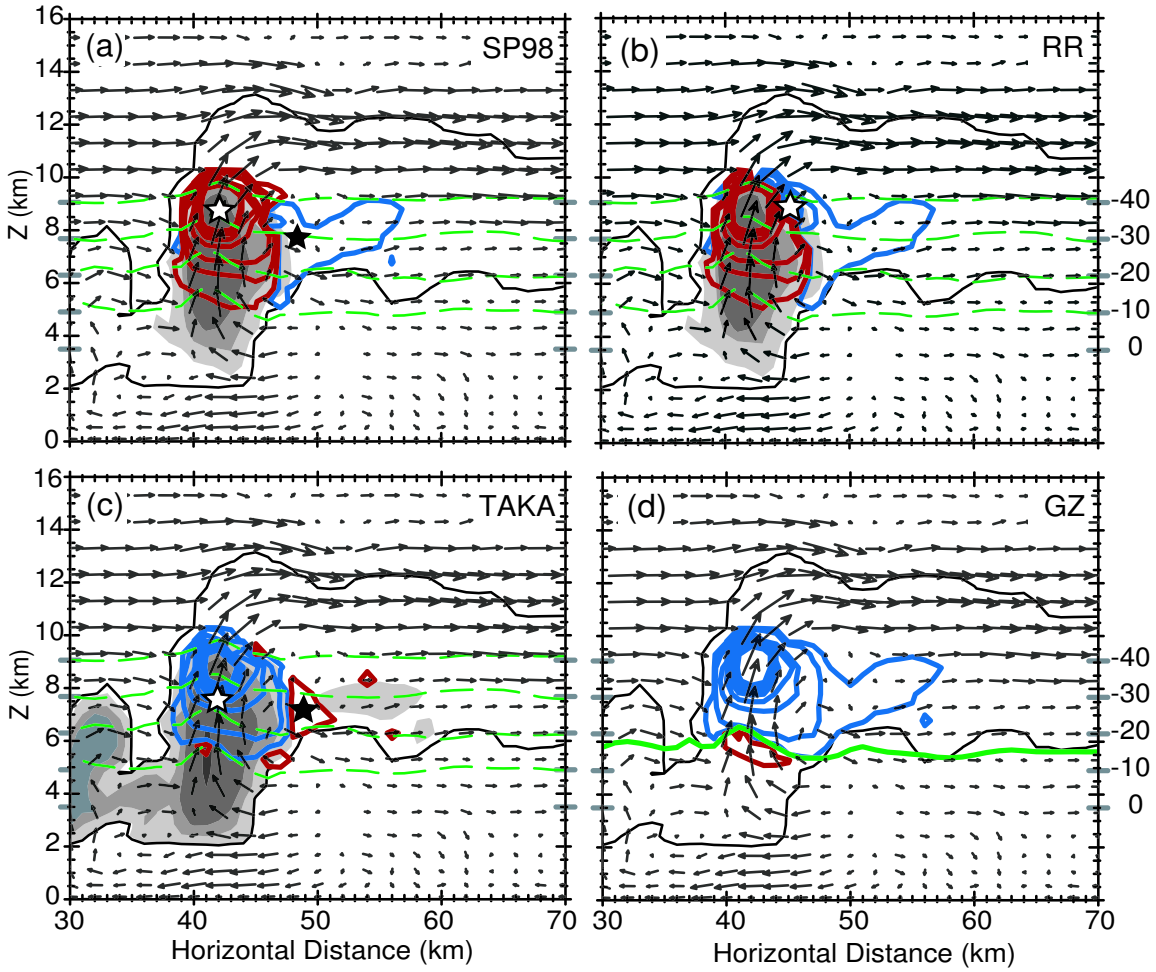

Figure 15: (a) Charging rate for SP98 at 76 min. Red contours signify positive charging in updraft region (maximum: $+$ 339.49 pC m^{-3} s^{-1}) , blue contours negative charging (maximum: $-$ 15.75 pC m^{-3} s^{-1}). Grey shading denotes the rime accretion rates for the area: 1, 4, 7 (g m^{-2} s^{-1}). Temperature levels shown by green dashes lines and cloud boundary shown in black. White and black stars correspond to same level of RAR and temperature shown in Fig. 2a. (b) Charging rate for RR at 76 min., all variables same as in (a). White star highlights difference between RR and SP98 charging corresponding with Fig. 2b. (c) Charging rate for TAKA at 76 min. Grey shading highlights different amounts of cloud water content ranging from 0.1, 0.5, 1, 2 g m^{-3}. Other variables same as in (a). (Maximum positive charging: $+$ 4.12 pC m^{-3} s^{-1}, Maximum negative charging: $-$ 314.76 pC m^{-3} s^{-1}) White and black stars correspond to the same level of liquid water content and temperature as in Fig. 2c. (d) Charging rate for GZ at 76 min, solid green line denotes -15°C level. Other variables as (a). (Maximum positive charging: $+$ 3.91 pC m^{-3} s^{-1}, Maximum negative charging: $-$ 338.94 pC m^{-3} s^{-1}). Same cross-section as shown in Fig. 11 panels (b), (e), (h), and (k).

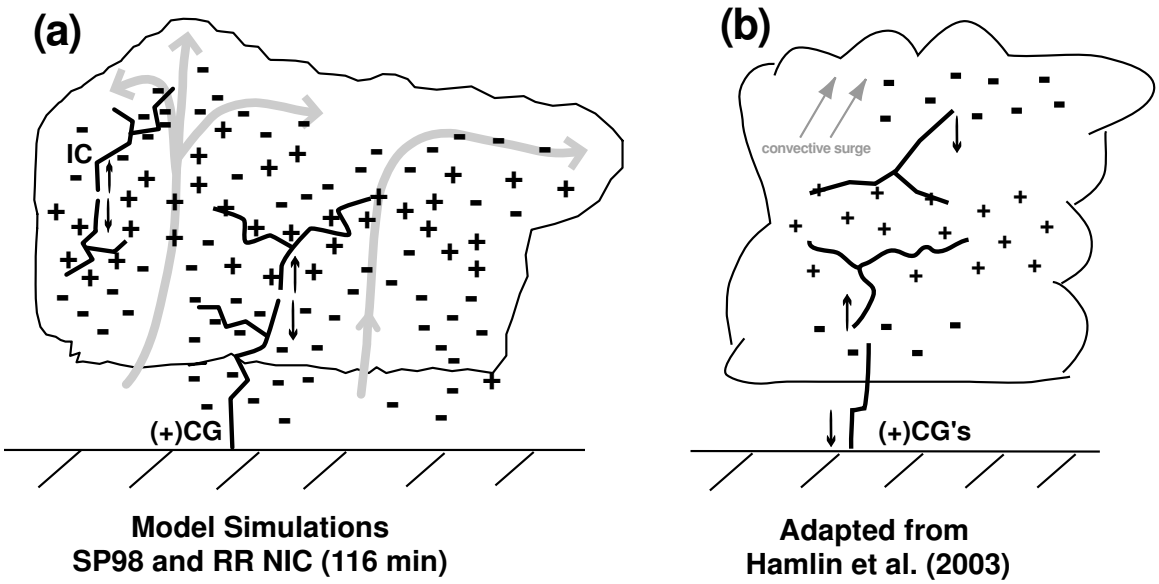

Figure 16: Charge structure from: (a) SP and RR simulations at 116 min, airflow shown by grey streamlines; typical IC and +CG in black (b) observations of 29 June once the storm had developed supercell characteristics, from Hamlin et al. (2003) Fig. 6 (far right) with leaders from LMA activity shown.

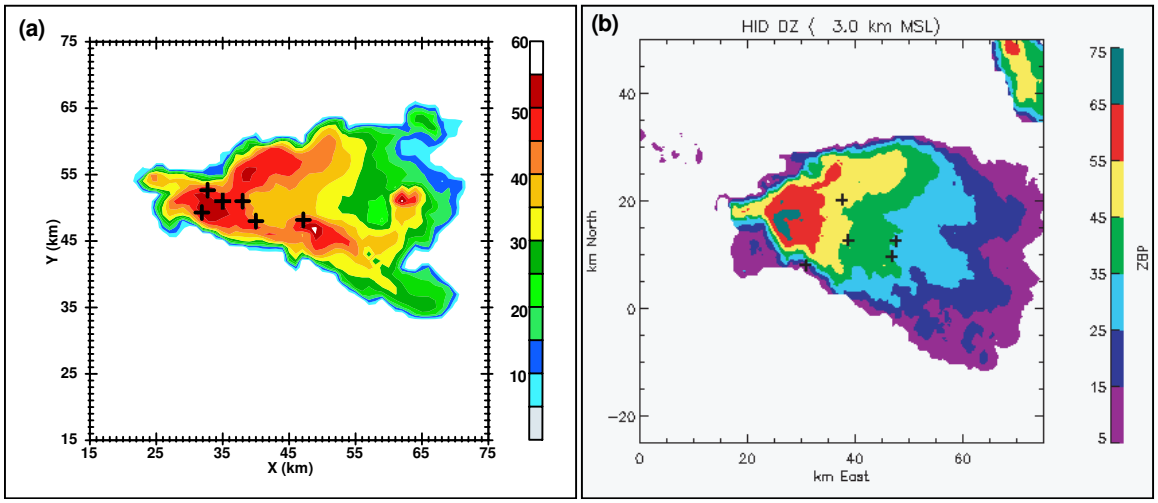

Figure 17: (a) Simulated storm reflectivity and ground flash location/polarity with SP98 scheme at 118 min. (b) Observed storm at 2357 UTC, SPOL dBZ at 3 km (from of K. C. Wiens, personal communication, 2004). Location where positive leader touched ground denoted by + symbol in both plots. Each depicts six minutes of lightning activity surrounding radar time.

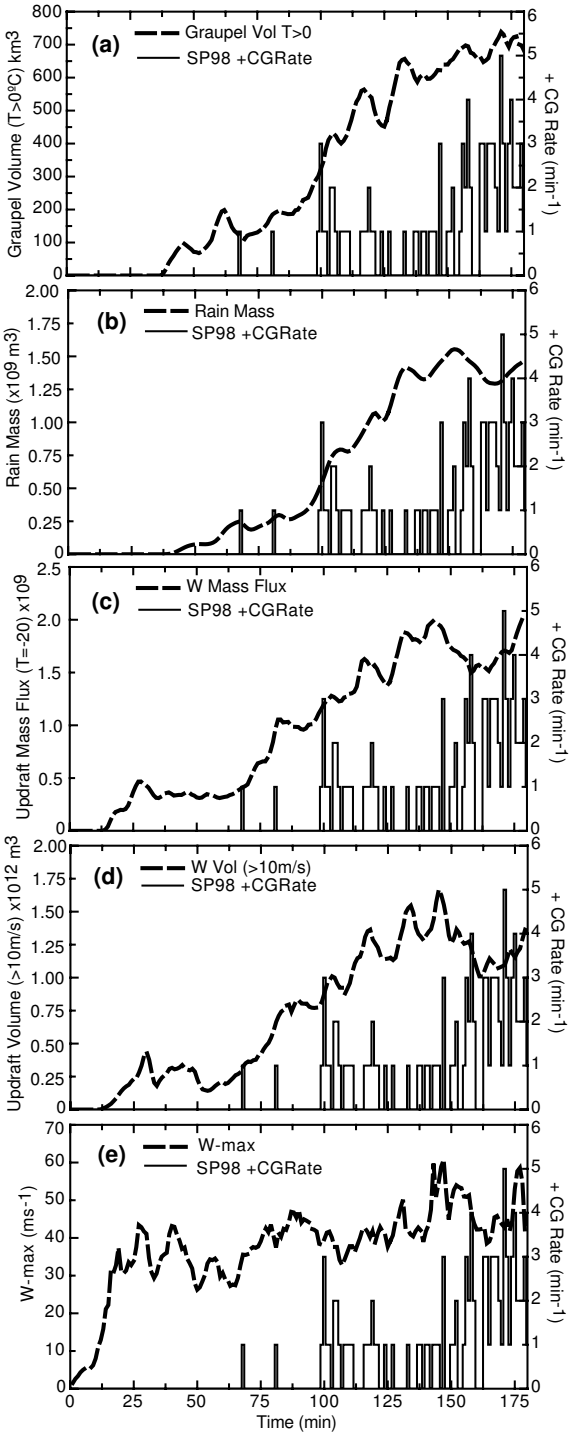

Figure 18: Time series: (a) Graupel volume at temperatures warmer than 0°C and positive CG rate from the SP98 simulation. (b) Rain mass (dashed line), positive CG rate from SP98 simulation; (c) Updraft mass flux through the T=20°C level (dashed line), positive CG rate from SP98 simulation; (d) Updraft volume greater than 10 m s^{-1} (dashed line) and positive CG rate from SP98 simulation; (e) Maximum updraft speed and positive CG rate from SP98 simulation.

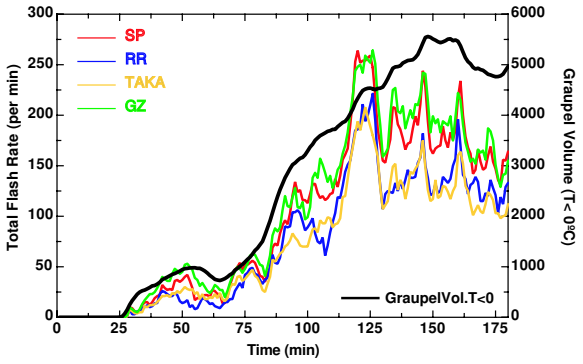

Figure 19: Time series: total flash rate per min from the simulations–SP (red), RR (blue), TAKA (yellow), GZ (green)–and graupel volume (black line, secondary y-axis).

List of Tables

Charging Scheme	Number of Flashes		
	Total (IC+CG)	+CG	−CG
OBS (LMA/NLDN)	10000	140	19
SP98	17274	98	0
RR	13243	128	0
TAKA	12678	0	63
GAR	18507	3	2

Table 1: Summary of total lightning for the observed storm and each simulation. Totals are for 180 min elapsed time from model initiation.

Microphysical Parameters	Total Flash Rate			
	SP	RR	TAKA	GZ
Graupel Volume ($T < 0°\mathrm{C}$)	0.770	0.706	0.721	0.808
Updraft Mass Flux ($T = -20°\mathrm{C}$)	0.533	0.482	0.513	0.561
Updraft Volume ($W > 10\,\mathrm{m\,s^{-1}}$)	0.650	0.595	0.626	0.686
W-max	0.091	0.090	0.098	0.075

Table 2: Correlations of total flash rate and microphysical parameters (Trend removed).